ULB UNIVERSITÉ LIBRE DE BRUXELLES

iihe BRUXELLES BRUSSEL

Faculté des Sciences
Département de Physique

Characterization of a Triple-GEM Detector Prototype for the CMS Muon Spectrometer Upgrade with GEM Detectors

Marco Zecchin

Promoteur : Dr. Gilles De Lentdecker

Année académique 2013-2014

Mémoire présenté en vue de l'obtention du diplôme de Master en Sciences Physiques (60 ECTS)

Résumé

Les détecteurs triple-GEM sont une technologie apte à intégrer la région frontale du spectromètre à muons du CMS, lors de la mise à niveau du LHC planifiée afin de permettre d'atteindre une haute luminosité ($2 \times 10^{34}\ cm^{-2}s^{-1}$). Ces détecteurs montrent une résistance très élevée aux importants flux de particules attendus dans cette région du spectromètre. Dans ce mémoire, j'ai testé un petit prototype d'un détecteur triple-GEM ($10 \times 10\ cm^2$) afin de caractériser son gain et son efficacité, en utilisant des photons issus d'une source de Fe^{55} et des muons cosmiques. Les mesures ont été réalisées gâce à un nouveau dispositif expérimental, encore en développement au service de physique des particules de l'ULB.

Abstract

The triple-GEM detectors are a candidate technology to instrument the forward region of the CMS muon spectrometer, during the upgrade of LHC scheduled to achieve high luminosity ($2 \times 10^{34}\ cm^{-2}s^{-1}$). These detectors show a very high resistance under the high particles fluxes expected in that region. In this work I tested a small triple-GEM prototype ($10 \times 10\ cm^2$) in order to measure gain and efficiency, using photons generated by an Fe^{55} source and cosmic muons. The measurements have been performed using a completely new set-up still in development at the ULB particle physics department.

Key-words: high energy physics, LHC, CMS, GEM, Upgrade, muon detector

Acknowledgment

I am very grateful to Dr. Gilles De Lentdecker for the time he devoted to me, as well as for the help and the relevant advises he gave me all along this work.

I am especially thankful to Florian, Jian, Patrizia, Ryo and Thierry for having patiently listened and answered my numerous questions and for the support they gave me. Furthermore, I would like to thank the other members of the GEM group at the IIHE for their congeniality and helpfulness.

I am in particular very thankful to my future wife Virginie, who encouraged me during the months of work and especially for the patience she had during my absences. Without her support I wouldn't have been able to accomplish this work.

Contents

Introduction

During the second long shutdown period of the Large Hadron Collider (LHC), the Compact Muon Solenoid Experiment (CMS) will be submitted at major upgrades. In particular the CMS GEM collaboration plans to instrument the forward region of the CMS muon spectrometer with triple-Gaseous Electron Multiplier detectors (GEMs). Such detectors are able to operate at high gain and high spatial resolution (100 μm) with the extreme particles rate expected in that region, during the high luminosity phase of LHC.

In this framework I tested a small triple-GEM prototype ($10 \times 10\, cm^2$) using a completely new experimental set-up still in development in the laboratory of the ULB particle physics department, at which I actively participated.

Chapter 1 describes the LHC machine and in particular the experience CMS, in order to present the framework of the CMS muon spectrometer and the scheduled upgrades.

Chapter 2 reminds the working principle of a gas detector and the avalanche amplification process.

Chapter 3 describes different kinds of modern Micro Pattern Gaseous Detectors (MPGDs) and in particular it details the triple-GEM detectors.

Chapter 4 presents the new experimental set-up where all the measurements have been performed.

Chapter 5 characterizes the triple-GEM detector under study and details the experimental framework. It gives also the obtained results in terms of gain and efficiency.

Chapter 1

Large Hadron Collider

The Large Hadron Collider (LHC) is the most powerful and largest high-energy particle collider built to date. It consists of a 27 km ring of superconducting magnets and accelerating structures to boost particles. It lies in a tunnel at about 100 m beneath the Franco-Swiss border near Geneva.

The LHC allows us to study matter under conditions never explored before and it is the state of the art in high-energy particle physics. Its extraordinary success is due to the strategy operated by the European Organization for Nuclear Research (CERN) since the end of the second world war, in order to bring Europe back to the top of the scientific community. The key points of this strategy are the cooperation between European states, which permit not only joining scientists but also sharing the increasing cost of the particle physics facilities, and the re-using of the already existing accelerator complex including the Large Electron Positron collider (LEP) tunnel.

1.1 Historical Introduction

The LHC was built by CERN from 1998 to 2008, but the official starting point is the symposium organized in Lausanne in 1984 [1]. It was clear that various aspects of high-energy physics could be studied with a proton-proton collider and the CERN Council approved the project in 1994 to begin construction in 1998. The first two experiment officially approved are the Compact Muon Solenoid (CMS) and the A Toroidal LHC ApparatuS (ATLAS) followed by two others,the Large Hadron Collider beauty (LHCb) and the A Large Ion Collider Experiment (ALICE). They represent the four main current detectors of the LHC.

During the first years the civil engineering works were the main task, meanwhile several parts of the detectors were apart conceived, built and tested. Starting from 2003 the several sections of the machine were assembled and in 2008, for the first time a proton beam circulated in the main ring of the LHC. Unfortunately an incident damaged the machine and delayed further operation for almost one year. In order to prevent other

incidents the beam energy is gradually increased and a series of shutdowns have been scheduled for upgrades and maintenance.

1.2 The Accelerator Complex

The accelerator complex is a succession of machines that accelerate particles to increasingly higher energies and the LHC is the last element in this chain. A schematic representation is depicted in Figure 1.1.

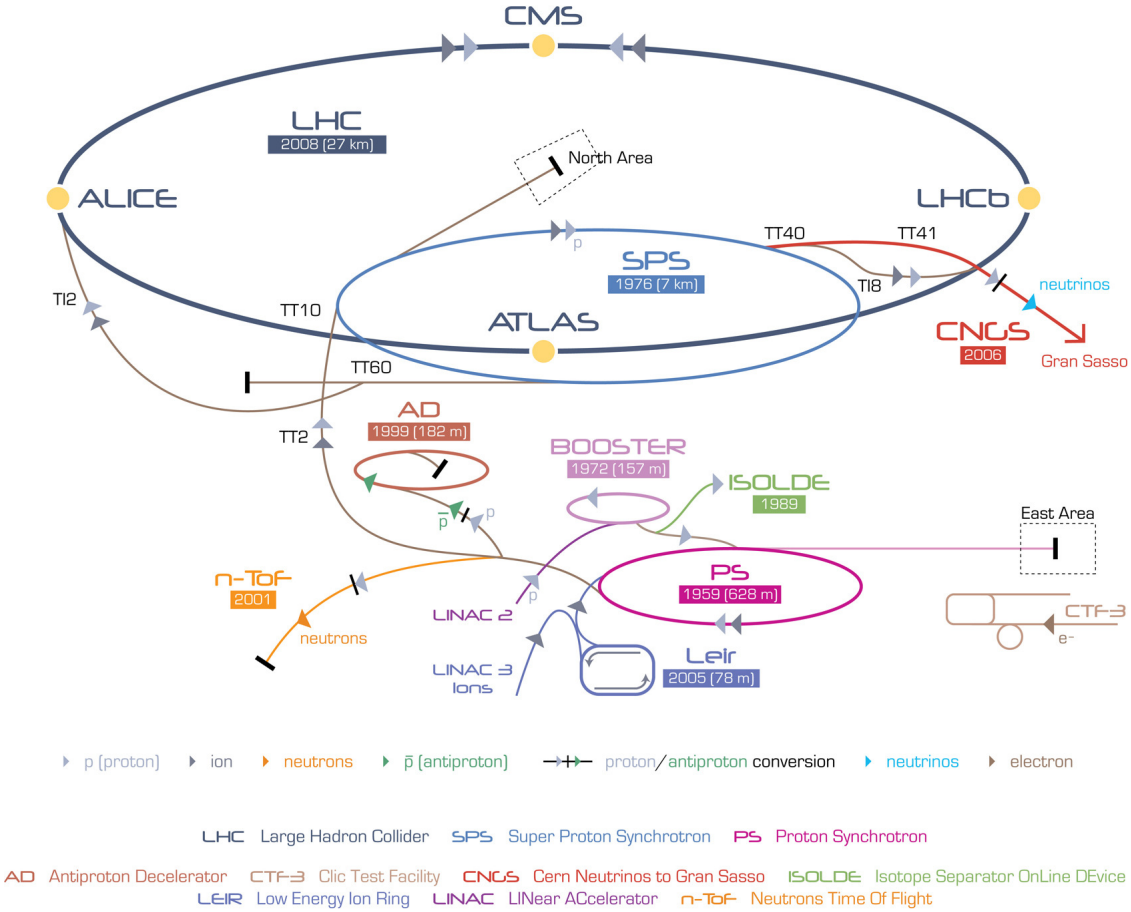

Figure 1.1 – A schematic representation of CERN accelerator complex [2]

The protons are produced by a source of ionized hydrogen gas and the first accelerator in the chain is the Linac2 which accelerates them up to 50 MeV. The beam is injected in the Proton Synchrotron Booster (PSB) that speeds up protons to 1.4 GeV, followed by the Proton Synchrotron (PS), which accelerates the beam to 25 GeV. The next accelerator in the chain, the Super Proton Synchrotron (SPS), increases beam's energy to 450 GeV and the protons are eventually transferred to the LHC in two different pipes where

they circulate in opposite direction.

Protons are accelerated by high-frequency electromagnetic waves in the radiofrequency (RF) cavities and the frequency is adjusted to have the appropriate polarity in order to accelerate the particles passing through. A consequence of this process is the regroup of the beam in bunches of particles.

1.3 Performance

The collision energy in the center of mass frame is a very important parameter in order to study the physics beyond the Standard Model (SM) and LHC has a nominal value of 14 TeV that, as mentioned before, will be gradually achieved. Nevertheless the energy is not the only relevant parameter; the luminosity is also an essential feature to detect rare processes.

The number of events per second depends on the instantaneous luminosity:

$$N_{event} = L\sigma_{event} \tag{1.1}$$

where σ_{event} is the process' cross section and L is the luminosity of the machine. The latter depends only on the beam parameters and if two bunches containing n_1 and n_2 particles collide head-on with a frequency f:

$$L = f\frac{n_1 n_2}{4\pi\sigma_x\sigma y} \tag{1.2}$$

where σ_x and σ_y are the rms of the transverse beam size, in the horizontal and vertical directions. In this forme it is assumed that the bunches are identical in transverse profile, that the profiles are Gaussian and that the particle distributions are the same during bunch crossing.

ATLAS and CMS are two high luminosity experiments and they aim at peak of luminosity (L) of $10^{34}cm^{-2}s^{-1}$, LHCb and the TOTal Elastic and diffractive cross-section Measurement experiment (TOTEM) aim at a lower luminosity peak, $10^{32}cm^{-2}s^{-1}$ for the former and $2\times10^{29}cm^{-2}s^{-1}$ for the latter. Regarding the experiment operating with ion beams, ALICE, the peak of luminosity will be of $10^{27}cm^{-2}s^{-1}$.

The exploration of rare events therefore requires high beam energies and high beam intensities. Some beam parameters are shown in Table 1.1 .

	Unit	Injection 450 GeV	Collision 7 TeV
bunch area $(2\sigma)^*$	eVs	1.0	2.5
bunch length $(4\sigma)^*$	ns	1.71	2.5
Energy spread $(2\sigma)^*$	$10*-3$	0.88	0.22
Intensity per bunch	$10^{11}p$	1.15	1.15
Number of bunches		2808	2808
Normalized rms transverse emittance V/H	μm	3.75	3.75
Intensity per beam	A	0.582	0.582
Synchrotron radiation loss/turn	keV	-	7
Longitudinal damping time	h	-	13
Intrabeam scattering growth time - H	h	38	80
Intrabeam scattering growth time - L	h	30	61
Frequency	MHz	400.789	400.790
Harmonic number		35640	35640
RF voltage/beam	MV	8	16
Energy gain/turn (20 min. ramp)	keV	485	485
RF power supplied during acceleration/ beam	kW	~ 275	~ 275
Synchrotron frequency	Hz	63.7	23.0
Bucket area	eVs	1.43	7.91
RF (400 MHz) component of beam current	A	0.87	1.05

Table 1.1 – Beam and machine parameters [2]

1.4 The Compact Muon Solenoid Experiment

The Compact Muon Solenoid (CMS) is one of the four main detectors of LHC and it is installed about 100 m underground. The detectors of CMS have to meet some essential requirements since the beam energy and the design luminosity of the LHC lead to an event rate of 10^9 events/s. This huge rate has to be reduced, with an online event selection process (trigger), to about 100 events/s. Moreover, the very short time between two bunch crossing, 25 ns, force to design and realize very efficient read-out and trigger systems.

Some of the principal requirements for the CMS detectors are:

- Good muon identification and momentum resolution over a wide range of momenta and angles, good dimuon mass resolution (≈ 1 % at 100 GeV/c^2), and the ability to determine un-ambiguously the charge of muons with momentum p $<$ 1 TeV/c;
- Good charged-particle momentum resolution and reconstruction efficiency in the inner tracker. Efficient triggering and offline tagging of τ's and b-jets, requiring pixel detectors close to the interaction region;
- Good electromagnetic energy resolution, good diphoton and dielectron mass reso-

lution (≈ 1 % at 100 GeV/c^2), wide geometric coverage, π^0 rejection, and efficient photon and lepton isolation at high luminosities;

- Good missing transverse energy and dijet-mass resolution, requiring hadron calorimeters with a large hermetic geometric coverage and with fine lateral segmentation.

The structure and the major components of CMS are depicted in figure 1.2.

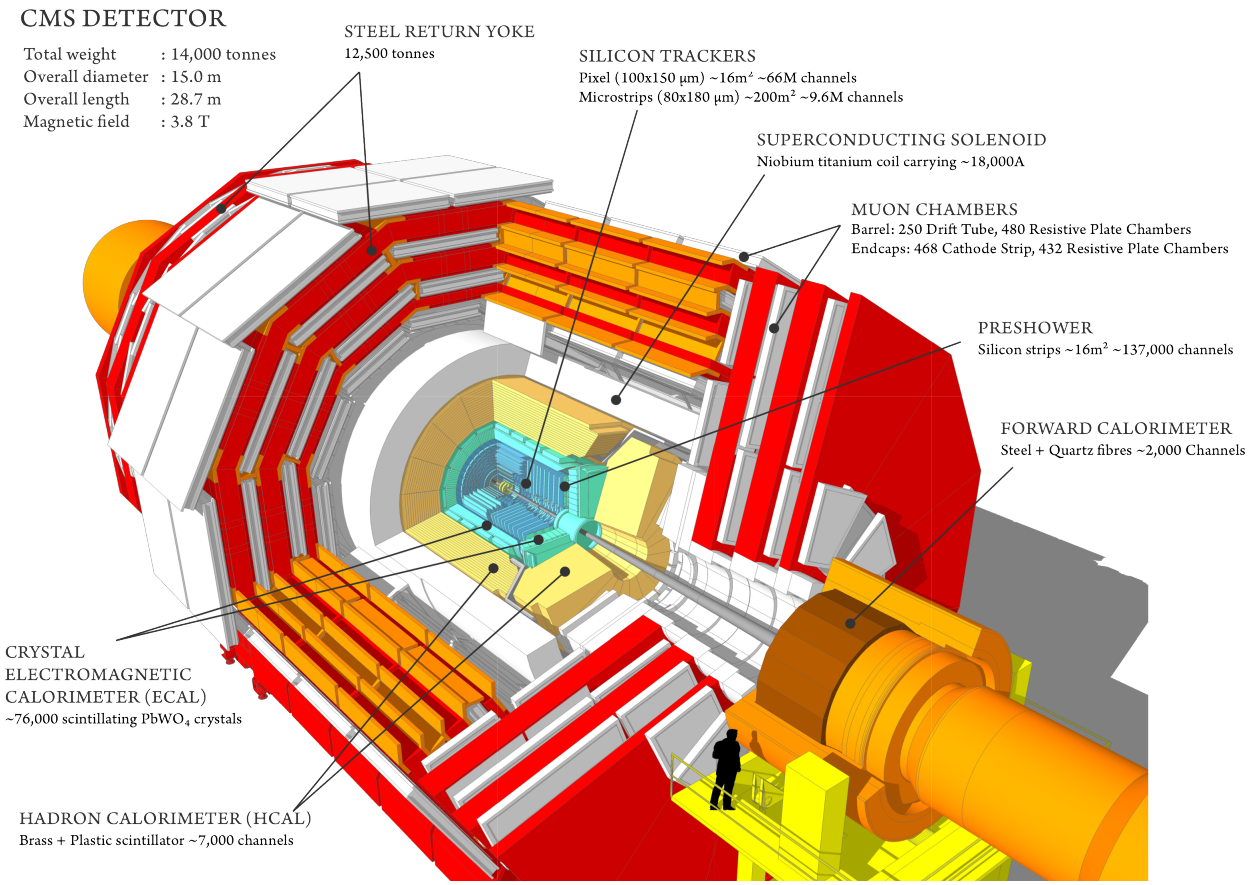

Figure 1.2 – 3D view of the CMS detector. The major components are shown. [3]

1.4.1 The CMS Coordinate System

It is very useful to define a convenient coordinate system for the CMS cylindrical detector. In the coordinate system adopted by CMS, the origin is located at the nominal collision point, inside the detector. The Z-axis points along the beam direction, the X and Y axis define a transverse plane. The X axis points radially to the center of the LHC circumference and the Y axis points vertically upward. The azimuthal angle ϕ measures the distance from the x-axis in the x-y plane, whereas the angle θ is the polar angle and

it is measured from the z-axis.

Another very important quantity is the pseudo-rapidity η, actually this is a convenient spatial coordinate to describe the angle between a particle and the beam axis. Pseudo-rapidity does not depend on the energy of a particle but only on the polar angle θ. The pseudo-rapidity is defined as:

$$\eta = -\ln\left[\tan\left(\frac{\theta}{2}\right)\right] \tag{1.3}$$

For highly relativistic particles, this is an good approximation of the rapidity's definition:

$$y = \frac{1}{2}\ln\left(\frac{E + p_z}{E - p_z}\right) \tag{1.4}$$

1.4.2 The Overall Layout of CMS

The overall layout of CMS is shown in figure 1.2, it has a length of 21.6 m, a diameter of 14.6 m and a total weight of 14500 tons. CMS is composed of several detectors and each one has a specific role in particles detection. A big superconducting solenoid sits at the heart of CMS, it is about 14 m long with a radius of about 3 m and it generates a magnetic field of 3.8 T which provides a good momentum resolution for high energy muons.

Inside the superconducting solenoid are installed the silicon tracker, the Electromagnetic CALorimeter (ECAL) and the Hadronic CALorimeter (HCAL), whereas the outside is dedicated to the muons detectors. Due to the shape of the solenoid, the detector is divided in two regions, a cylindrical barrel and two planar endcaps.

In the following sections, the different detector systems will be briefly described.

1.4.3 Tracking

The inner tracking system of CMS is the closest detector to the interaction point, it provides a precise and efficient measurement of the trajectories of charged particles and it allows getting an extraordinary spatial resolution of 25 μm. At the LHC design luminosity about 1000 particles are generated at each bunch crossing, namely every 25 ns, therefore, an high granularity and a fast response is mandatory. However these features are a technological and financial challenge. The CMS tracking system consists of two main parts, the silicon pixel and the silicon strips detectors [4]. A schematic representation is given in figure 1.3.

The pixel detector provides a similar track resolution in both ϕ and z direction, with a pixel size of 100 $\times$ 150 μm^2. The pixel detector covers a range of pseudo-rapidity of

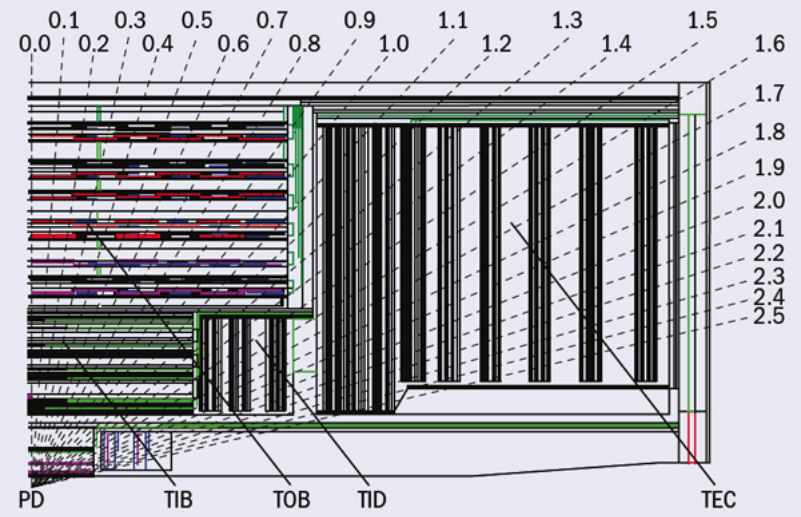

Figure 1.3 – A schematic representation of a quarter of the tracking system. It is subdivided into the Pixel Detector (PD) and the microstrips. The microstrip system includes the Tracker Inner Barrel (TIB), the Tracker Inner Discs (TID), the Tracker Outer Barrel (TOB) and the Tracker EndCaps (TEC) [5].

$|\eta| < 2.5$ and it consists of three barrel layers (BPix) with two endcap disks (FPix). This detector is essential for the reconstruction of secondary vertices. In figure 1.4 a silicon pixel detector is shown, each pixel has its own readout electronics.

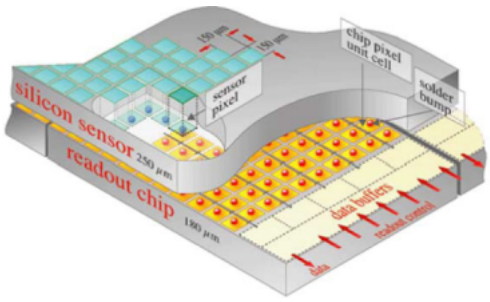

Figure 1.4 – Schematic view of the pixel sensor [4]

The CMS Silicon Strip Tracker (SST) is made by silicon modules and each one is equipped with sensors and the readout electronics. The modules are arranged in layers and disk around the pixel detector. The SST is separated in a Tracker Inner Barrel (TIB), inside, and in a Tracker Outer Barrel (TOB), outside. In the forward region there are the Tracker Inner Disks (TID) and the Tracker End Caps (TEC), as shown in figure 1.3. Using silicon strips only one coordinate is measured and the granularity is lower then the pixel detector, in order to reduce the data that have to be collected. The consequence is a good resolution, $\approx 53\ \mu m$, perpendicularly to the strips, but a low resolution along

the strips corresponding to the size of the detection strip.

1.4.4 Calorimeters

The aim of the calorimeters is to absorb the full kinetic energy of a particle, creating particle cascades. In CMS there are two kinds of calorimeters, the Electromagnetic CALorimeter (ECAL) and the Hadronic CALorimeter (HCAL).

1.4.4.1 Electromagnetic Calorimeter

The Electromagnetic CALorimeter (ECAL) is located around the tracker detector and it is inside the solenoid. The goal is to measure the energy of particles like electrons and photons, which are electromagnetically interacting. Through interactions with matter they produce electromagnetic showers which are amplified and detected.

1.4.4.2 Hadronic Calorimeter

The Hadronic CALorimeter (HCAL) is placed around the ECAL. A first part is located inside the solenoid, the inner barrel region, a second part is inside the iron return yoke of the magnet [4]. The detector is completed by two end caps and two forward calorimeters, giving at the HCAL an hermetic design. The absorber material is copper and the emitting active material are made of plastic scintillators. Wavelength-shifters are used to route the signals to the end cap region to be read. The electrical signals are amplified by the electronics and the energy of the hadrons interacting with nuclei in the copper can be determined.

1.4.5 Muon System

Except the neutrinos, the muons are the only particles which can pass through the calorimeters without being absorbed. They are involved in many interesting processes and their detection is mandatory to discover and study new physics.

For the reasons mentioned before, the CMS muon system is placed in the outer region of the detector, where the muons are the only detectable particles left. The currently CMS muon system is composed of three different gas detectors: the Drift Tubes (DT), the Cathode Strip Chambers (CSC) and the Resistive Plate Chambers (RPCs). The DT are paced in the barrel region ($|\eta| < 1$), the CSC are situated in the end caps regions ($1 < |\eta| < 2.4$), whereas the RPCs are used in both parts. In figure 1.5 the disposition of the detectors is shown.

1.4.5.1 Drift Tubes

Due to the relatively low magnetic field in the barrel, the drift chambers can be used as tracking detector. A drift tube of 4.2 cm wide is composed of an anode wire stretched within a gas volume and placed between two cathode strips. A charged particle, passing

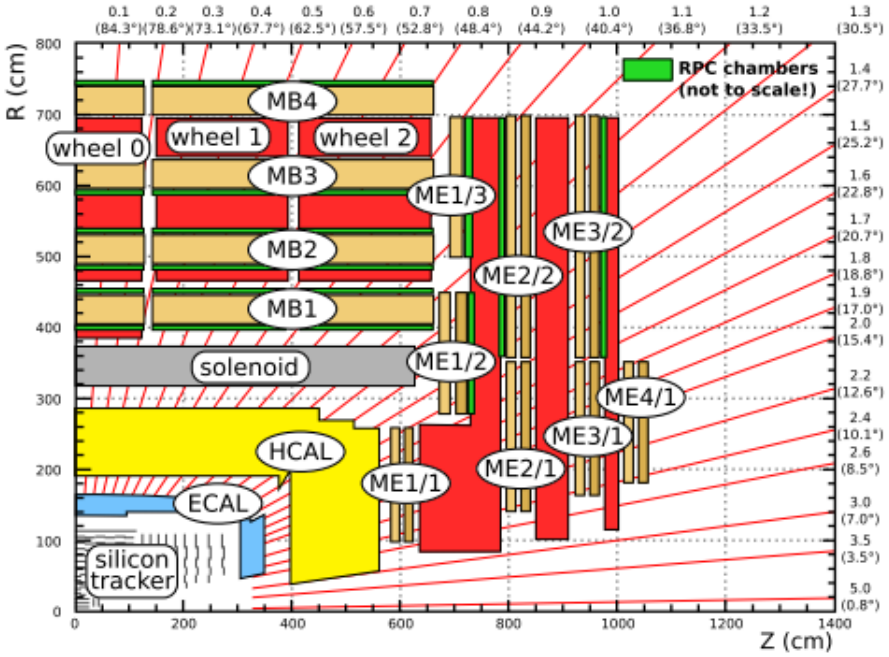

Figure 1.5 – Cross-section of a quadrant of CMS detector. The DTs are identified by MBn, the CSCs by MEα/β and the RPCs are in green [6].

through the gas, ionizes it creating an avalanche in proximity of the anode which will be amplified by the high voltage applied. In figure 1.6 a drift cell is sketched.

1.4.5.2 Cathode Strip Chambers

The CSCs are trapezoidal multiwire proportional chambers, made of 6 anode wire planes placed among 7 cathode planes. Their working principle is similar to the DTs, the signals come from the avalanches generated by gas ionization. Strips are housed into the cathode planes and run lengthwise. There are typically 80 strips spaced from each other by a distance varying from 8.4 mm, in the narrow part, to 16 mm in the larger part. There are instead about 1000 wires spaced by 3.2 mm which are stretched radially as we can see in figure 1.7 .

In figure 1.8 the placement of the CSCs is highlighted.

The muon coordinate along the wires is obtained by interpolating the charges induced on strips and the spatial resolution is 33 μm for ME1/1 and ME1/2, whereas it is only 80 μm for the other stations.

The CSCs provide many interesting features such as:

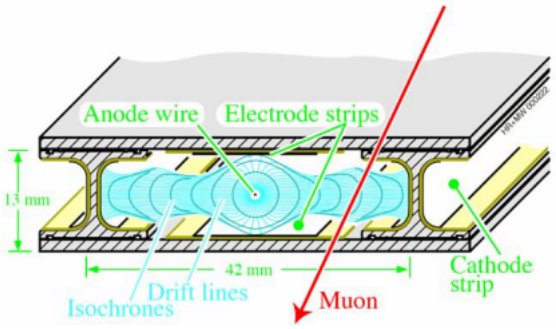

Figure 1.6 – Sketch of a drift cell. The voltage applied to the electrodes are +3600V for wires, +1800V for electrode strips and -1200V for cathode strips. [7]

- The precision muon momentum measurement and the muon trigger signal are provided by one device;
- The possibility to operate at high particle rates and in large and non-uniform magnetic fields, like in the endcaps of CMS;
- They do not require precise gas, temperature and pressure control;
- They can be easily arranged to fit the endcap shape;
- Low-maintenance operation for at least 10 years.

1.4.5.3 Resistive Plate Chambers

A complementary trigger system, consisting of Resistive Plate Chambers (RPC), was added in the barrel and in the endcaps regions. They provide a fast response with a good time resolution of 1 ns, but a poor spatial resolution of about 1 mm. They ensure a good operation at high rates, up to 1 kHz cm^{-2}, necessary to reach the full LHC's luminosity.

The RPCs are gaseous parallel-plate detectors which consist of 2 gaps of a few millimeters, formed by two parallel bakelite plates with a bulk resistivity from 10^{10} to $10^{11}\Omega cm$ and a schematic representation is depicted in figure 1.9 . The gap is filled with a freon-based gas mixture. The outer side of the plates are coated with conductive graphite in order to create the Hight Voltage (HV) required and to ground the electrodes.

The charged particle ionize the gas and initiates the electron cascade which will be amplified by the HV applied. The drift of electrons to the anode induce a charge on the strips and generate an output signal.

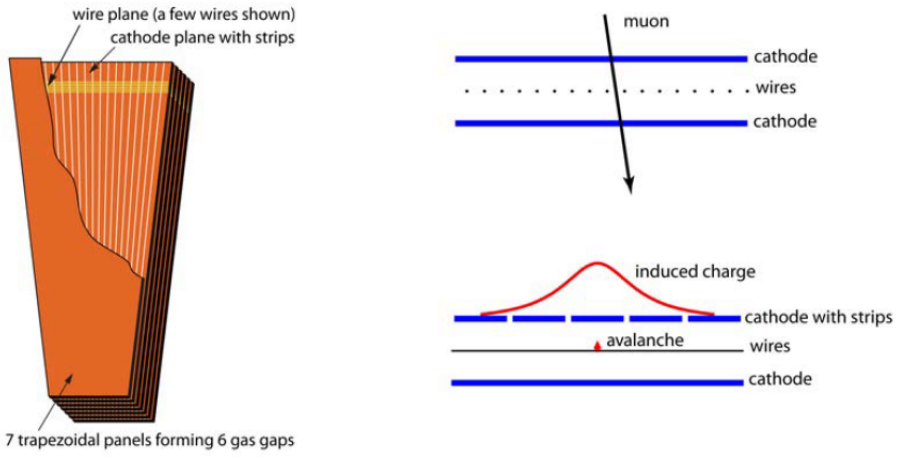

Figure 1.7 – Layout of a trapezoidal CSC (left) where only a few wires are shown. A schematic view of a single gap illustrating the working principle of a CSC (right) [7]

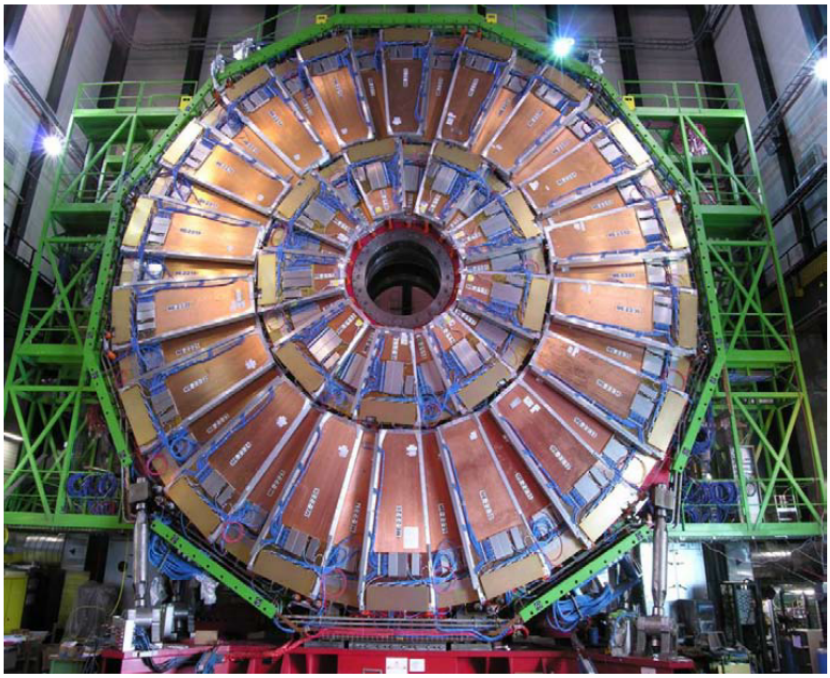

Figure 1.8 – The ME2 station of CSCs. The chambers overlap to provide contiguous coverage in ϕ [7].

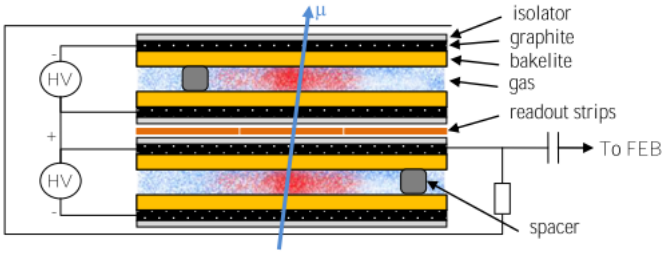

Figure 1.9 – Cross-section of a RPC chamber [8].

1.5 Upgrade and Future Operations

According to LHC operational plan for the next ten years running, the operational time of the machine is interleaved with shutdowns periods. The first long shutdown period has begun in 2013 and the LHC accelerator complex is currently being upgraded. The major intervals can be summarized as follows [6]:

- **(2010-2012) 7 TeV operation:**
  To commission the LHC and the experiments and make early measurements of physics at this energy, with a restricted luminosity up to $5 \times 10^{33}\ cm^{-2}s^{-1}$;
- **(2013-2014) Long Shutdown 1 (LS1):**
  To repair magnet splices to allow the LHC to operate safely at 14 TeV and to improve collimation to permit operation at high luminosity;
- **(2015-2016) 14 TeV run:**
  To explore Terascale physics at nominal luminosity up to $10^{34}\ cm^{-2}s^{-1}$within the capability of existing detectors;
- **(2017) Long Shutdown 2 (LS2):**
  To improve collimation in the LHC to enable operation at highest luminosities, up to $2 \times 10^{34}\ cm^{-2}s^{-1}$. Major upgrade of the muon spectrometer is required and in particular the possibility to install triple-GEM detectors;
- **(2018-2020) 14 TeV high luminosity run:**
  To explore Terascale physics and to study in more details new phenomena observed in the preceding runs using the upgraded detectors;
- **(2021-2023) Long Shutdown 3 (LS3):**
  Major upgrade in order to reach a luminosity of $5 \times 10^{34}\ cm^{-2}s^{-1}$.

1.5.1 LS1 Upgrade

All the CMS subdetectors will benefit from this break by improving important features to operate at higher energies and collision rates.

The new Linac4 will replace the Linac2 as injector to PS Booster (PSB). The new Linac will increase the beam intensity and eventually the LHC luminosity [9].

At the end of the LS1, the energy will be gradually increased up to 14 TeV, using the whole magnets capability, at nominal luminosity. The luminosity will be further increased during the High Luminosity (HL) era, after the LS2.

1.5.2 LS2 Upgrade

The second phase of the upgrade will be realized around 2018. Two new injector-accelerators, the Superconducting Proton Linac (SPL) and the Proton Synchrotron 2 (PS2), will replace the PS Booster and the PS, respectively [9]. They allow getting a factor of 2 in the ultimate beam luminosity.

1.5.2.1 Muon System upgrade

Muon detection is a powerful tool for recognizing signatures of interesting processes and in particularly when the luminosity increases; therefore major upgrades of this system are planed [6].

To maintain robust performance of the CSC system, even during the High Luminosity (HL) phase after the LS2, an increased redundancy of the system is required. In order to achieve this goal, a new station ME4/2 and an upgrade of the station ME1/1 is scheduled. Several electronics components have to be replace in order to maintain the the CSC trigger and reconstruction efficiencies.

In the DTs the readout and trigger electronics will be changed to sustain the radiation and to increase the bandwidth and the readout speed of the modules.

The current RPCs modules have to be replaced to maintain the detection efficiency required, during the HL phase. Some alternatives are under study and the CMS GEM Collaboration suggests to instrument with Gaseous Electron Multiplier (GEM) detectors, in the most forward part of the CMS muon spectrometer, $1.6 < |\eta| < 2.1$. The present work is performed in this particular framework.

Chapter 2

Gaseous Detectors

Gaseous detectors offer various advantages and they are extensively used in high energy particles physics. The most important features are:

- Limited quantity of sensitive material (gas), useful to avoid multiple diffusion and to reduce the energy loss;
- They are a relatively cheap technology, which makes them very attractive to cover large areas;
- Relatively light and robust and hence easy to integrate in an existing system.

The working principle, which will be reviewed in details in this chapter, is the following. A charged particle, passing through the gaseous detector, ionize the gas. Electrons and ions are drifted apart by the electric field present inside the detector and the electrons create further electrons-ion pairs in an avalanche process. Through the avalanche process, the number of electrons is multiplied, typically by several thousands, in order to make the signal detectable by the readout electronics.

2.1 Gas Ionization

An energetic charged particle which traverses a gas can ionize it. We can then distinguish between two kinds of events, the primary and the secondary ionization [10]. In the case of the primary ionization, along their flight path in the gas, the energetic particles interact with the atoms of the medium A and eject one or more electrons from them. For a π meson interacting with an atom A we can observe:

$$\pi + A = \pi + A^{+} + e^{-}, \pi + A^{++} + e^{-} + e^{-}, \ldots \tag{2.1}$$

However, most of the charge along a track is created by the secondary ionization. In this case, the electrons coming from the primary ionization have enough energy to ionize the gas in turn, generating a secondary ionization:

$$e^{-} + A \rightarrow e^{-} + A^{+} + e^{-} \tag{2.2}$$

There are several other processes that can occur when an energetic particle passes through a medium, such as the Auger effect. In the Auger effect, the electron ejected comes from an inner shell of the atom and another electron, from higher orbitals, takes its place emitting a photon which can escape or ionize the medium in turn.

Only a fraction of the total amount of energy lost by the incoming particle is spent in ionization. Every gas mixture is therefore characterized by a mean energy W, necessary to ionize the medium:

$$W \langle N_l \rangle = L \left\langle \frac{dE}{dx} \right\rangle \tag{2.3}$$

where $\langle N_l \rangle$ is the average number of ionization electrons created, L is the length of the trajectory and $\left\langle \frac{dE}{dx} \right\rangle$ is the average total energy loss per unit path length.

The value of W has to be measured experimentally. Table 2.1 reports some data for various gases. The energy W depends on the composition and density of the gas and on the nature of the particle.

Gas	Density, $\mathrm{mg\,cm^{-3}}$	E_x eV	E_I eV	W_I eV	$dE/dx\|_{\min}$ $\mathrm{keV\,cm^{-1}}$	N_P $\mathrm{cm^{-1}}$	N_T $\mathrm{cm^{-1}}$
Ne	0.839	16.7	21.6	30	1.45	13	50
Ar	1.66	11.6	15.7	25	2.53	25	106
Xe	5.495	8.4	12.1	22	6.87	41	312
CH_4	0.667	8.8	12.6	30	1.61	37	54
C_2H_6	1.26	8.2	11.5	26	2.91	48	112
iC_4H_{10}	2.49	6.5	10.6	26	5.67	90	220
CO_2	1.84	7.0	13.8	34	3.35	35	100
CF_4	3.78	10.0	16.0	54	6.38	63	120

Table 2.1 – Main parameters for several gases [11].

The average number of ionizations per unit of length is hence given by:

$$n = \frac{1}{W} \left\langle \frac{dE}{dX} \right\rangle . \tag{2.4}$$

For example, using the values reported in table 2.1, we can compute the total number of ion pairs produced by minimum ionizing particles in pure Argon:

$$n_{Ar} = \frac{\Delta E}{W_{Ar}} = \frac{2.5 keV/cm}{25 eV} \approx 100\ pairs/cm \tag{2.5}$$

In the prototype tested in the present work, the zone where the main signal is formed has a thickness of 3 mm. Therefore in that region, a minimum ionizing particle, like cosmic-ray muons, produces only 30 electrons. Impossible to be detected by the readout electronics without a strong amplification process.

2.1.1 Stopping Power in Matter

In the case of moderate relativistic charged particles, the energy loss per unit of length of traversed material is well-described by the following Bethe equation [12]:

$$-\left\langle \frac{dE}{dx} \right\rangle = Kz^2 \frac{Z}{A} \frac{1}{\beta^2} \left[\frac{1}{2} ln \frac{2m_e c^2 \beta^2 \gamma^2 T_{max}}{I^2} - \beta^2 - \frac{\delta(\beta\gamma)}{2} \right] \tag{2.6}$$

This is the mean rate of energy loss for particles with $0.1 < \beta\gamma < 1000$ and for intermediate Z materials. T_{max} is the maximum kinetic energy which can be imparted to a free electron in a single collision. Z is the atomic number of the absorber, A its atomic mass, z is the charge of the incident particle, m_e the electron mass, r_e the classical electron radius, I the mean excitation energy (eV), $\delta(\beta\gamma)$ is a density effect correction to ionization and $K = 4\pi N_A r_e^2 m_e c^2$.

The mean ionization potential I has a value of about 10 eV, and it is actually difficult to calculate, it is estimated starting from dE/dx experimental measurements.

The equation 2.6 is valid for several types of charged particles. Figure 2.2 illustrates the behavior of mean energy loss for muons in copper as function of $\beta\gamma$, that is p/Mc, since relativistically $p = Mv\gamma = M\beta\gamma c$. The stopping power in other materials is shown in 2.3.

At low energy, $\beta\gamma < 1$, the velocity of the particles is comparable with the orbital electron speed of the absorber, increasing the stopping power of the material. The Bethe formula shows a minimum around $\beta\gamma = 3$, particles with this velocity are called Minimum Ionizing Particles (MIPs). At higher energies, $\beta\gamma > 10$, the mean energy loss is considerably affected by the density of the material. The effect is due to the alteration of the classical field of the passing particle by the electrical polarization of the medium.

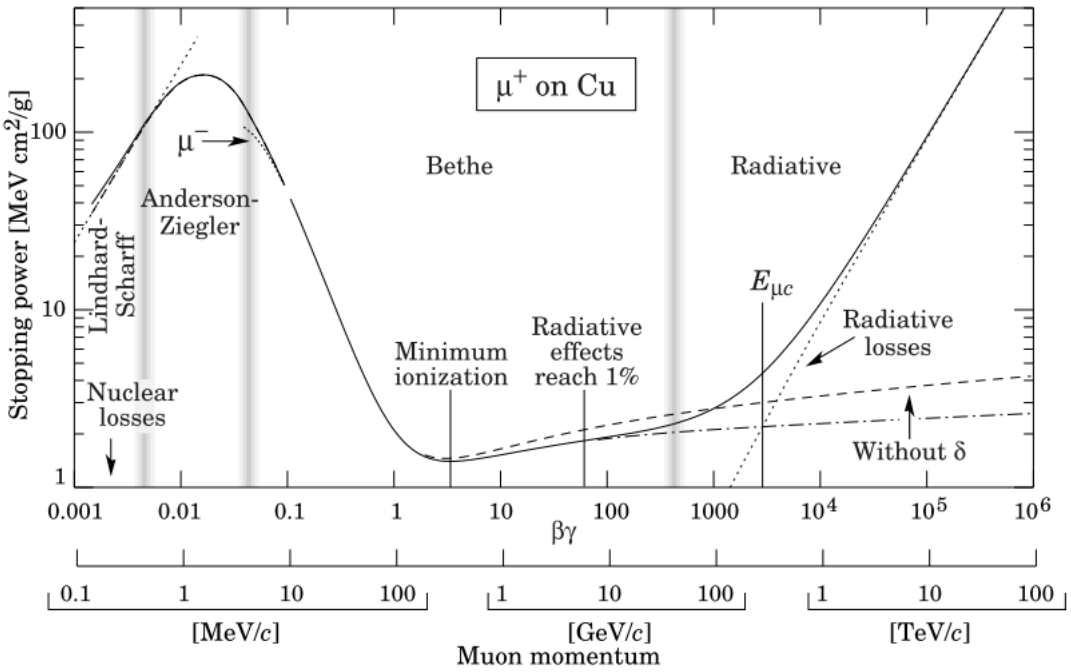

Figure 2.2 – Stopping power for positive muons in copper as function of $\beta\gamma$ [12].

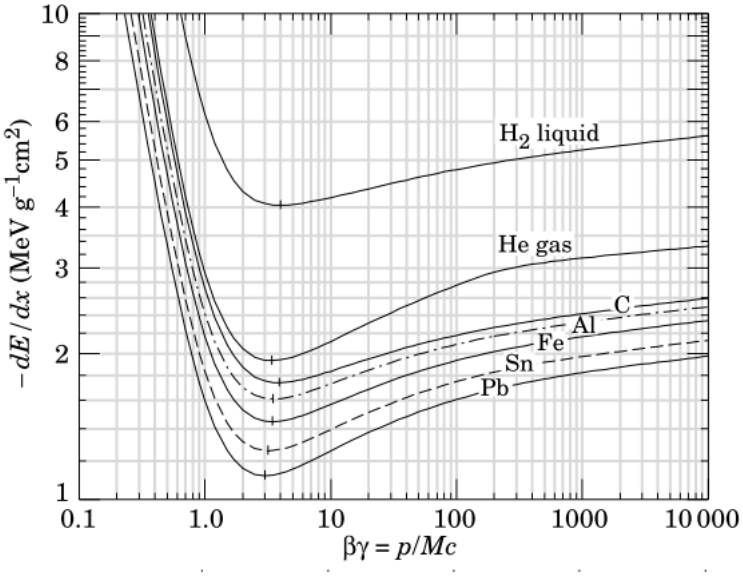

Figure 2.3 – Mean energy loss rate per unit of length, normalized to the density of the medium as function of the $\beta\gamma$ [12].

2.2 Signal Amplification

The very small number of electrons generated by primary and secondary gas ionization, is not able to produce a detectable signal. Effectively the noise generated by the readout electronics would completely mask the faint signal and an amplification process is therefore required. The amplification is obtained creating a strong electric field inside the chambers which allows electrons to gain enough energy to ionize the medium and create avalanches.

2.2.1 The Avalanche Process

When an external electric field provides enough energy to the electron ejected from the ionized atom, this drifted electron can ionize the medium in turn and this generates a cascade. In figure 2.4 a schematic representation of the process is shown.

Increasing the electric field, up to a few kV/cm, the energy distribution of the drifting electrons extends beyond the threshold of inelastic collision, resulting in excitation and ionization of the gas molecules.

The ionization produces an electron-ion pair and the two electrons can generate further ionizations in turn.

The amplification factor, called gain G(x), is defined as :

$$G(x) = \frac{N_x}{N_0} \tag{2.7}$$

where N_x is the total number of electrons created after a distance x and N_0 is the amount of primary electrons.

For ionization, the mean free path is defined as the average distance an electron has to travel before to be involved in an ionizing collision. The inverse of the mean free path is called the first Towsend coefficient α and it represents the number of ions pairs produced per unit length of drift.

It has to be noticed that the electrons move much faster than ions. Due to the small mass of the electrons, the electric field increases their energy between collisions with the gas molecules. Whereas the ions are almost stopped at each collision.

The multiplication factor can not be increased at will. The charge separation produced by the avalanche, as shown in figure 2.4 right, generates an electric field against the other already present inside the detector. This effect on one hand limits the multiplication process and on the other hand can produce secondary processes, like the emission of photons due to ions and electrons recombination. At that point, a secondary avalanche,

spread over the gas volume, can produce a spark breakdown. This phenomenon can seriously damage the detector and should be avoided. A way to reduce the probability of such breakdown is to use mixtures of gases. Gases like CO_2 or CF_4 have several excitation levels and, if added in the gaseous mixture, they can easily absorb the secondary photon produced by the recombination. The gases added are called «quenchers» for their capability to absorb photons.

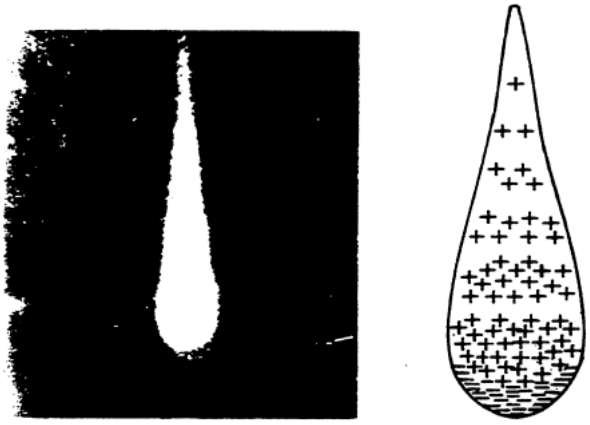

Figure 2.4 – Representation of a drop-like shape avalanche. The ions leave behind the fast electron front [13].

2.3 The Gas Mixtures

The gas mixture is one of the most important feature of a gas detector and different compounds lead to different detector properties. For instance, the drift velocity of electrons in the medium depends on the gas nature as well as the gain, the rate capability and the working voltage. In most cases, the peculiar requirements of each experience restricts the choice of the gas mixture.

Noble gases can only be excited through photon absorption or emission, while polyatomic molecules have radiationless transitions of rotational and vibrational nature, therefore they are used as quencher. The dissipation of a good fraction of energy in that transitions is capital to get high gain. We can notice that the avalanche multiplication occurs in noble gases at much lower fields than in the other molecules [13], therefore the use of noble gases as the main component is a good choice. Between the noble gases, Argon is the best choice because it has a high specific ionization and it is cheep. As mentioned before, discharges can seriously limit the gain in such a counter. Even small amounts of polyatomic quencher added to the Argon results in a very efficient ion ex-

change and in a suppression of the secondary emission, leading at gain up to 10^6.

For these reasons, the gas mixture used during the tests on the triple-GEM prototype presented in this work is $Ar - CO_2$ 70-30 %.

Chapter 3

Micro Pattern Gaseous Detectors

In this chapter the various Micro Pattern Gaseous Detectors (MPGDs) are briefly described and in particular the Gas Electron Multiplier (GEM) detector. The GEM detector will be described in more details since the prototype tested in this work is precisely a triple-GEM detector.

3.1 Multiwire Proportional Chambers

The space resolution of a single wire proportional counter is very limited, and for that reason the MultiWire Proportional Chambers (MWPC) have revolutionized the field of the particles detectors.

A MWPC consists essentially of a set of thin, parallel and equally spaced anode wires, placed between two cathode planes. Figure 3.1 shows schematic views of MWPC. When a negative potential is applied to the cathodes, an electric field is present between the wires and the plates and the field lines are shown in figure 3.1 (b) and (c). When some charges are liberated after an ionizing event, the electrons will drift along the field lines approaching the high field region in proximity of the anode wires. At this point the avalanche occurs and the signal can be recorded through the readout electronics connected to the wire.

For each positive induced signal in one anode wire, there is another negative signal, produced by capacitive coupling, in the other parallel non-screened wires. The presence of this signal in all wires could compromise any spatial resolution for a multiwire structure. In 1968 Charpak and collaborators recognized that the induced signal is much less intense then the one produced by the avalanches and in this way, each wire can be considered an independent counter.

MWPC are still important component of many particle detectors, however they suffer of a rate capability limitation. The rate capability is limited to a value of 10^4 Hz/mm^2

which is lower than the requirements of modern high energy particle physics.

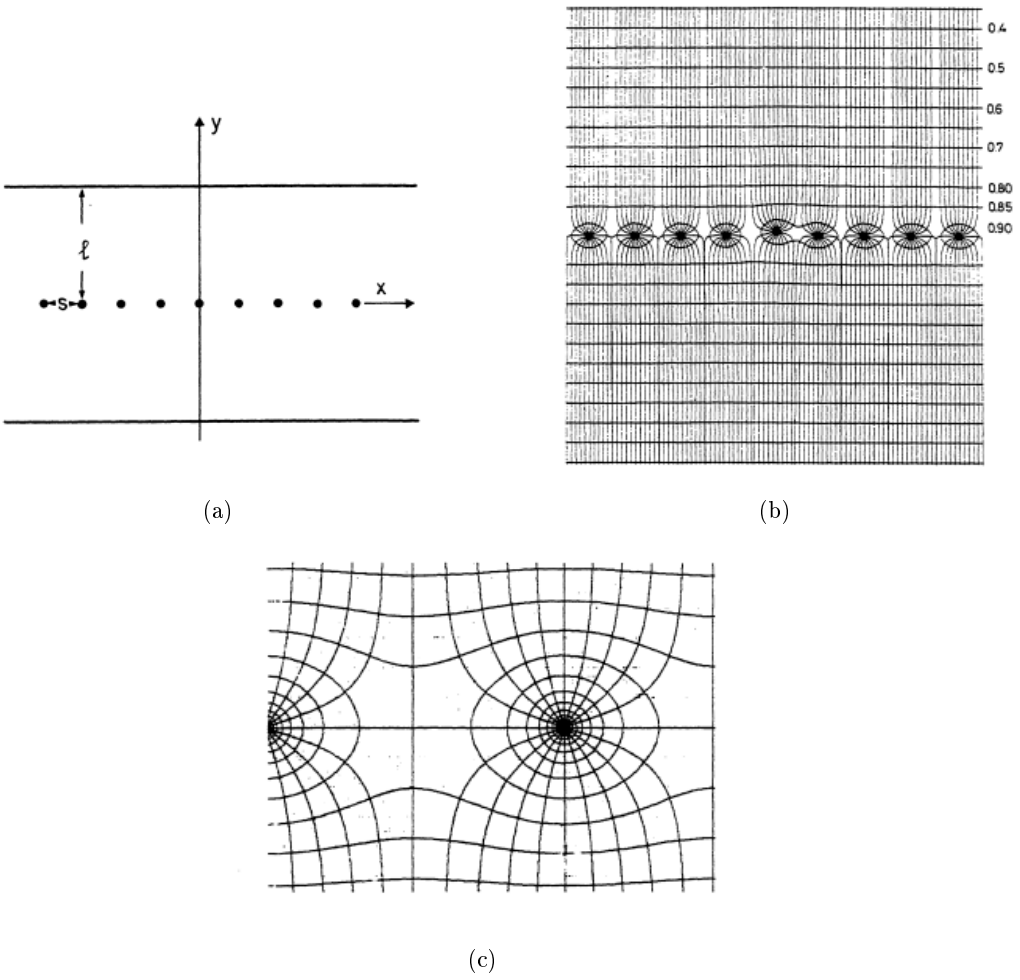

(a) (b)

(c)

Figure 3.1 – In figure (a): set of parallel anode wires between two cathode planes in a MWCP. In figure (b): field lines in a MWCP. In figure (c): enlarged view of the field around the anode wires. [13]

3.2 Micro Pattern Gaseous Detectors

In order to obtain higher rate capability than the MWPCs, a new sort of detectors was developed: the Micro Pattern Gaseous Detectors (MPGD). They consist typically in planar structures that generate, in various ways, the intense electrical field required by the amplification [14]. In particular, the amplification field is not generated by wire

structures but with very narrow gap of 50-100 μm. In figure 3.2 different patterns and the corresponding field lines are shown.

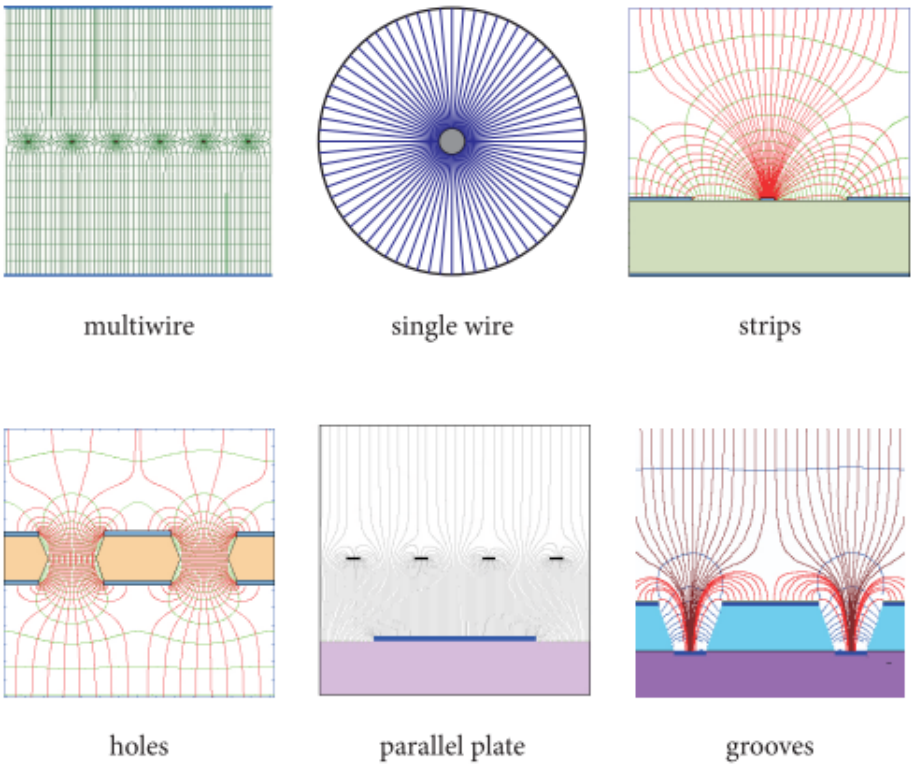

Figure 3.2 – Patterns of different gas detector technologies and the corresponding field lines.[14].

3.2.1 Microstrip Gas Chambers

A Microstrip Gas Chamber (MSGC) resembles a MWPC but fine printed strips replace the thin wires, see figure 3.2 upper right. Using microelectronics techniques, it is possible to realize very narrow gap between anode strips of about 200 μm, to compare with the several millimeters spacing in the case of wire chambers.

In MSGC the cathode strips are spaced from the anode strips by only 60 μm an the ions created during the avalanche drift to them very quickly, whereas, in the MWPC, ions could remain longer in the gas mixture and modify the electric field and the gain in turn. This charge effect, which limits the rate capability of multiwire chambers, is hence strongly reduced in MSGC and in micro pattern detectors in general. The high rate capability makes these detectors an attractive technology for high-energy and nuclear physics.

On the other hand, there are some typical issues and limitations for MSGC and micro pattern detectors such as the charging of insulating surfaces and discharges. The latter is the most important issue with MSGC technology and can lead to fatally damage of the detectors. The Gas Electron Multiplier (GEM) was introduced to solve this problem. A preamplification stage allowed the GEM to work at lower voltage with a lower probability of discharges.

Since the prototype which we tested is a triple GEM detector, it will be described in details in section 3.5.

3.2.2 Micromegas

The Micromesh Gas detector (Micromegas) consists in a parallel micromesh plate, and the amplification is generated in the gap between the plates and the readout board. They have a narrow amplification gap of 50-100 μm, as depicted in figure 3.3. The most important features are fast signals and high rate capability.

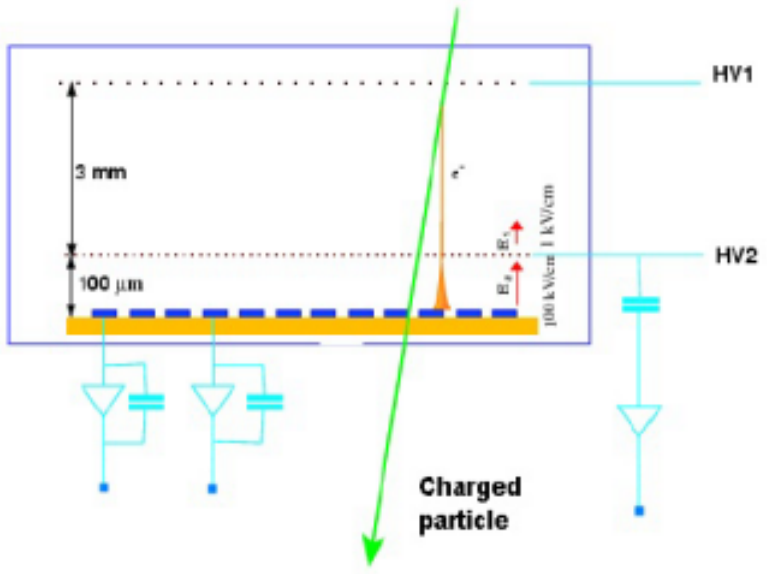

Figure 3.3 – Schematic view of a micromegas detector [14].

3.3 Construction Techniques for Micropattern Gas Detectors

The industry of microelectronics and printed circuits provides the main techniques to build up the MPGDs, such as photolithography, metal etching and screen printing. In particular the etching of polyimide has been refined and employed at CERN in order

to realize GEM detector prototypes. Using these techniques it is possible to create a multitude of structures which are convenient for various applications. In figure 3.4 some images of various detector structures are reported.

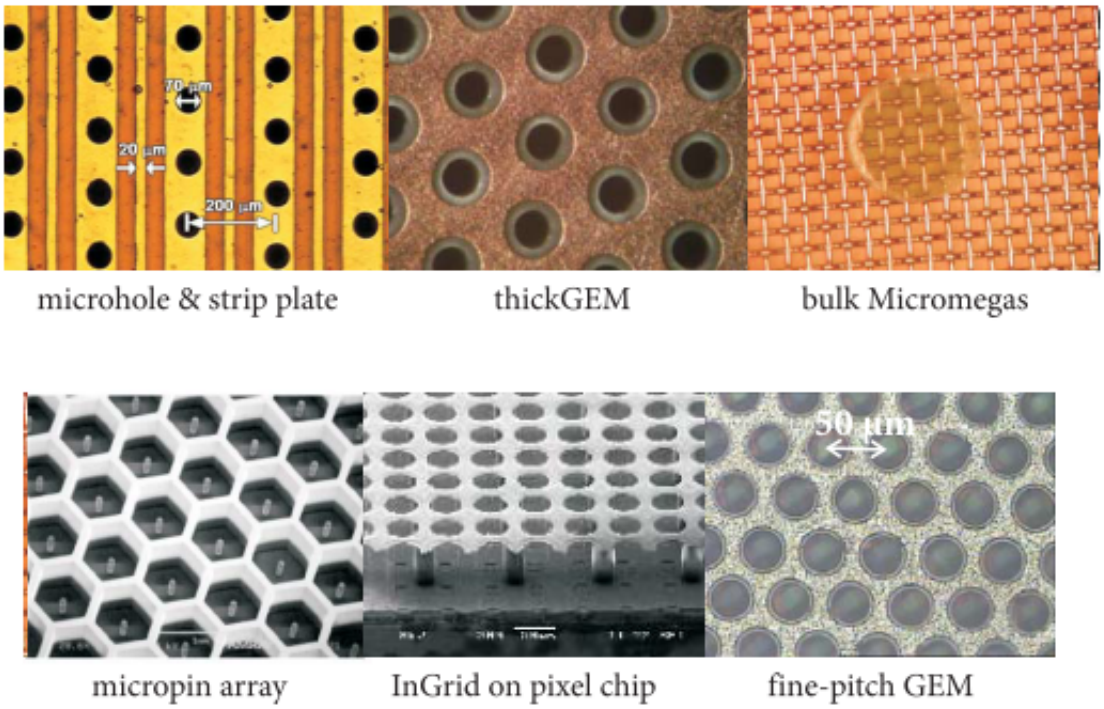

Figure 3.4 – Various detector structures [14].

3.4 Applications of MPGDs

The MPGDs have a wide field of applications, from science to industry, they are used in high-energy and nuclear physics, synchrotron and thermal neutron research and medical imaging [14]. At CERN they are especially used in the COMPASS experiment, in LHCb and TOTEM experiments and they are foreseen for upgrade of the LHC experiments: ALICE, ATLAS and CMS.

3.5 Gas Electron Multiplier Detectors

The Gas Electron Multipliers (GEMs) are gaseous detectors with a good spatial resolution of order 100 μm, excellent time resolutions of a few ns, a detection efficiency above 98 % and a rate capability up to 10 MHz/cm^2. The last is a very important feature since it makes GEMs detectors suitable for the upgrade of the CMS muon system. During the high luminosity phase, the $1.6 < |\eta| < 2.4$ region should be instrumented with additional

detectors in order to maintain the present performance level, in particular in terms of tracking and triggering. In that region, for the high-luminosity phase of LHC, particle rates of several kHz/cm^2 are expected and the CMS GEM Collaboration aims at complete the muon system with additional layers of triple-GEMs. This kind of detectors can operate indeed at high gains and in stable manners, even in high radiation environments.

3.5.1 Description and Working Principle

GEM detectors are a relatively recent technology, developed for the firs time by CERN in 1998, they are composed of a thin insulator foil of Kapton of 50 μm, coated with a 5 μm copper layer on each side. The Kapton is a polymide film, it is a good insulator which remains stable in very wide range of temperature and it is largely employed in printed circuits and electronics.

As all the MPGDs, the GEM detectors working principle is based on the ionization of the gas by charged particles. Small holes are made using photolitography processes and they are equally spaced on the GEM foil. They have typically a diameter less then 100 μm and a pitch of 140 μm, see figure 3.5. The signal generated during the primary and secondary ionization process, is amplified in the GEM hole by the high electric field between the top and the bottom of the copper layers as shown in figure 3.6. The electric field inside the holes is especially high, several tens of kV/cm, and it leads at huge gains of several thousands.

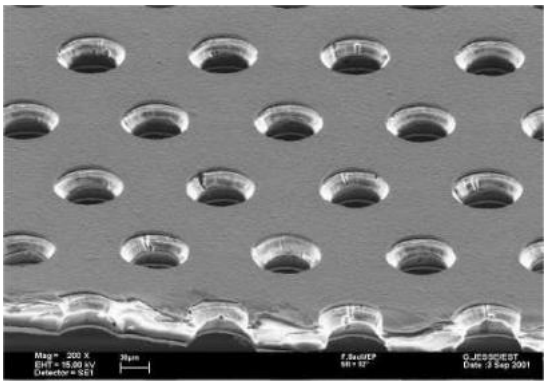

Figure 3.5 – Magnified view of a GEM foil showing the hole pattern with 70 μm outer diameter, 50 μm inner diameter, and 140 μm pitch [15].

The simplest GEM detector is made up with only one GEM foil and so called single GEM. Electrons, released by ionization in the gas on one side of the foil, drift into the holes and they are multiplied and transferred to a collection region. The electrons created through the GEM, then drift, over a couple of millimeters, in the collection region before reaching the readout plane, equipped with micro strips. These anodes have typical pitch

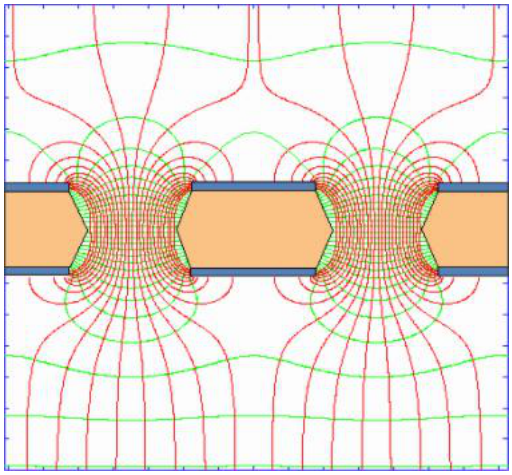

Figure 3.6 – Cross sectional view of two holes in a GEM foil showing electric field lines (red) and electric equipotential lines (green) [15].

of few hundreds of microns and they are readout individually by a preamplifier. The read-out plane offers also the possibility of two dimensional measurements as shown in figure 3.7.

In order to achieve the high gain necessary in most of the experimental setups, a very high voltage is applied across the GEM. In this condition, the probability of fatal discharge is relevant and to reduce it, the GEM detector is in general employed in a multiple structure. In this case the amplification is shared over the different GEM foils and this permits to obtain high total gain, with a relatively low voltage on each GEM foil. Therefore, multiple GEM foils structure are preferred since the discharge probability is strongly reduced.

The triple-GEM detector consists of a drift zone, where the primary ionization takes place, three GEM foils, spaced by a few mm, forming two transfer zones and a final induction zone. In the transfer zone, the electrons are driven to the following GEM foils to start the next amplification process. Whereas, the induction zone is the place where the signal is registered by the readout strips. A schematic view is given in figures 3.8 and 3.9 .

Another significant parameter for a GEM detector is the transparency, namely the ratio between the ingoing and the outgoing electrons in a GEM foil. The real gain of the GEM depends on this parameter which depends on the electric field lines. In a weak drift field, only a few field lines terminate on the upper GEM electrode, most of them pass through the holes and allow to achieve high gain. Increasing the drift field we obtain higher gains until a certain limit, after that, there are more and more field lines which terminate on the upper layer and the electrons are not driven through the holes but they are captured by the copper layer.

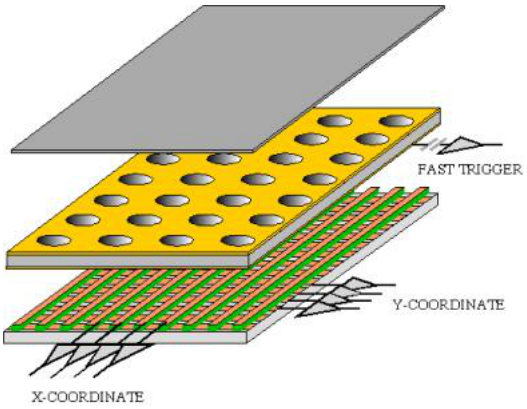

Figure 3.7 – Schematic view of a single GEM detector [15].

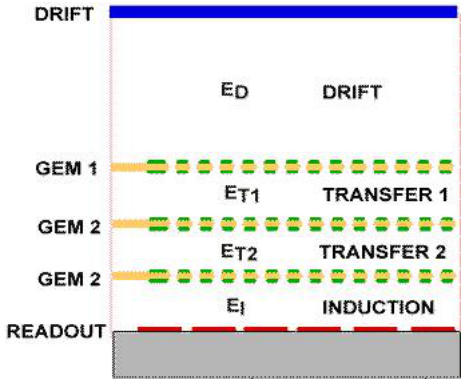

Figure 3.8 – Schematic view of a triple-GEM detector. The gain is shared between the foils [15].

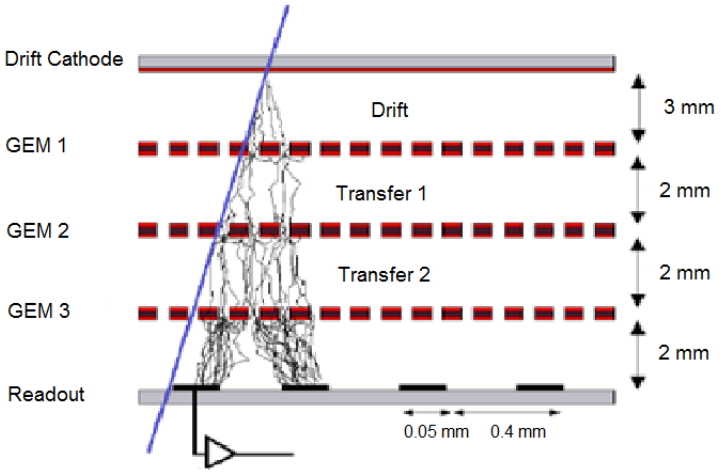

Figure 3.9 – Schematic view of a triple-GEM detector where the amplification process is shown [15].

Chapter 4

The Experimental Set-up: The Cosmic Arch

All the measurements of this work have been performed at the particle physics department of the ULB using a new experimental set-up: the cosmic arch. This chapter will describe in details the facility and introduce the main electronics that will be used all along this work.

4.1 Structure

The cosmic arch is an installation which allows the detection of cosmic rays, in particular muons. Using timing measurements the arch can be used to determine the comic rays zenith angle distribution. This facility will be used in the future to study the response of detector prototypes as a function of the incident muons' angle.

In Figure 4.1 is depicted the arch setup. The arch is composed of a wood structure forming an arch with a diameter of 398.3 cm. On this structure lie eight scintillator strips derived from the target tracker module of an already existing experiment, the Oscillation Project with Emulsion-tRacking Apparatus (OPERA) [16]. The light is collected by 16 Wave Length Shifting fibers (WLS fibers) and directed to PhotoMultipliers (PMs) where an analog signal is sent to specific electronic modules, the Nuclear Instrumentation Module (NIM).

On each side of the ribbon there are 8 blue LEDs and in proximity of them it is possible to fix a moveable plastic detector equipped with own PM. Such features make easier calibration and efficiency measurements.

4.1.1 The Scintillator Strips

The plastic scintillator strips are obtained by extrusion with a reflective coating of titanium dioxide (TiO_2) to improve light collection and in figure 4.2 a schematic view is

Figure 4.1 – The arch setup with the central table, useful to place other detectors.

shown. In the center of each scintillator strip there was originally a groove of 2.0 mm deep and 1.6 mm wide which has been enlarged to house two Wave Length Shifting fibers (WLS fibers), see figure 4.3. The fibers have been glued inside the groove using a high transparency glue. Eight bars, 7 meters long, have been cut in small rods of 12.8 cm long in order to fit the geometry of the arch and they have been arranged in 8 rows of 40 rods on the external side of the arch, as Figure 4.4 shows. The detector has finally a ribbon length of 516.9 cm, a width of 21 cm and there are 16 WLS fibers of 604 cm each. The fibers are routed at both ends of the arch where they are read by two photomultipliers, which we define as PM1 and PM2.

The PMs adopted are two *Hamamatsu H6780* with a gain of 106 and a rise time of 780 ps, table 4.1 lists the major details.

4.1.2 Central Modules

In the center of the arch there is an apposite site to place others detectors, this is a very useful feature since firstly it allows performing the calibration of the arch and sec-

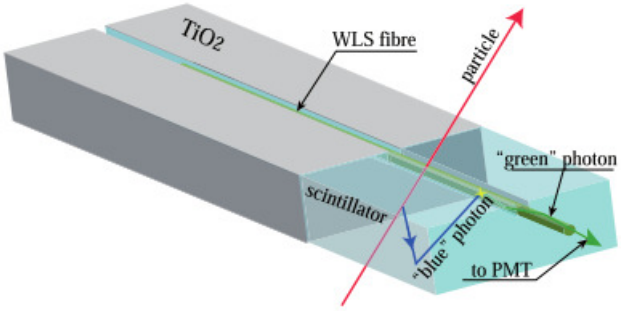

Figure 4.2 – Schematic view of a scintillating strip [16]

Figure 4.3 – WLS fibers inside the scintillator strips.

PM	**Model**	**Gain**	**Raise time**	**Transit time spread**
PM1 & PM2	Hamamatsu H6780	106	780 ps	230 ps
PM3 & PM4	Hamamatsu R7400	106 (850 V)	780 ps	230 ps
PM5	Photonis XP3102	5 × 105 (900 V)	2 ns	23.8 ns

Table 4.1 – PMs' relevant specifications

Figure 4.4 – External side of the arch with the scintillator ribbon installed.

Detector	Dimensions (cm)	PM	Moveable
sc-bot	21 × 21 × 2	2 Hamamatsu R7400	No
sc-top	21 × 21 × 2	Photonis XP3102	Yes

Table 4.2 – Central modules

ondly it provides an effective tool to realize measurements on small prototype detectors.

We have at our disposal a plastic scintillator, which will be further referenced as bottom scintillator (sc-bot), read by a two face-to-face *Hamammatsu R7400* PMs. Another plastic scintillator read-out by a single *Photonis XP3102* can be moved around the arch or laid on the central table, over the bottom scintillator. This movable scintillator will be further referenced as top scintillator (sc-top) and it is visible on the left hand-side of the arch in figure 4.1. More details about these detectors are listed in table 4.2.

4.1.3 Electronic Instrumentation

The signals coming from the PMs are sent to specific electronic modules: the Nuclear Instrumentation Modules (NIM). NIM defines a standard about electronics modules used in experimental particle and nuclear physics; it provides a standard footprint for electronic modules such as amplifiers, discriminators, timing electronics, high voltage power supplies, Analog to Digital converters (ADCs) and Digital to Analog Converters (DACs). The concept of modules in electronic systems offers several advantages, for instance more flexibility, the opportunity of interchange instruments and it makes easier the design. The

NIM standard defines also cabling, connectors, impedances and levels for logic signals.

We have at our disposal an CAEN N470 high voltage power supply, a low threshold discriminator CAEN N417, a Time to Digital Converter (TDC) CAEN V1290A, a dual timer CAEN N93B, a counter (quad scalar and preset counter-timer N145) and a logic unit (CAEN double manual programmable logic unit).

The CAEN N470 high voltage power supply :

The unit has 4 indipendent High Voltage (HV) channels able to supply four output voltages from 0 up to $\pm$ 8 kV [17].

Low threshold discriminator CAEN N417:

The discriminator generates precise logic pulse in response to input analog signals exceeding a given threshold. In figure 4.5 we can see the analog signal generated by a PM and the corresponding square signal of -800 mV generated by the discriminator.

The discriminator in use is a NIM module equipped with 8 independent non-updating discriminating channels. Each channel accepts both negative and positive input signals in the range from 1.5 mV to 250 mV, however the module in use is set to accept only negative signals. For each channel the threshold value can be set in above mentioned range through a trimmer placed on the front panel. The output signal width is adjustable, via a front panel control, in the range from 15 ns to 800 ns [18].

The Time to Digital Converter (TDC):

A Time to Digital Converter is a device which detects events and provides a digital representation of the arrival time of the signal. We use the TDC in trigger matching mode, in this mode hits are reported if they occur within a programmable matching interval. The trigger matching can be set through some programmable parameters: the match window, the window offset, the extra search margin and the reject margin. In channel 4 (Ch 4), the signal comes directly from the timing unit and starts the matching time window. The window offset is the interval between the trigger and the start of the trigger matching window and in this device must be subsequent to the match window. The trigger is represented by the delayed signal which indicates when the event of interest occurs. Starting from this trigger time, until the end of the trigger matching window, all hits issue from Ch 0 and Ch 1 will be considered as matching the trigger. There is also an extended search window to guarantee that all matching hits are found [19]. A timing diagram of this mode is

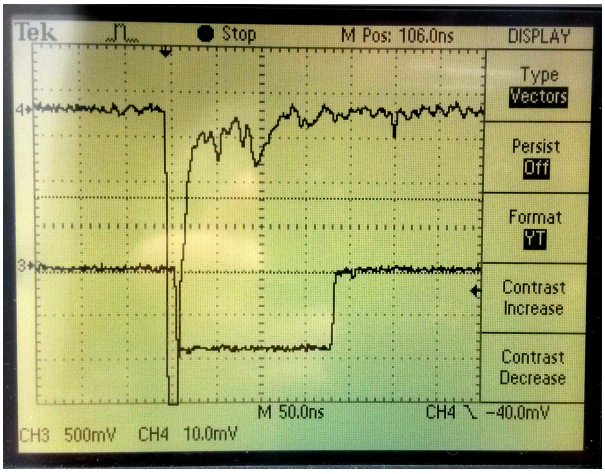

Figure 4.5 – The analog signal and the digital one generated by the discriminator with a threshold of -30 mV.

shown in figure 4.6.

When programming the matching parameters, two cases should be taken into account. In the first case, the trigger matching window precedes the trigger arrival and the window offset is negative, as shown in figure 4.7. In the second case, the matching window is in correspondence with the trigger or delayed with, and the window offset can be either negative or positive, as shown in figure 4.8. Accordingly with the instrument specifications, in the first case, the window width and the window offset have to be programmed following the relation:

$$\text{Match window width} < |\text{window offset}| \leq 4095 \text{ clock cycle} = 102375 \text{ ns}.$$

whereas in the second case we have:

$$\text{Match window with} + \text{window offset} \leq 40 \text{ clock cycles} = 1000 \text{ ns}.$$

The dual timer CAEN N93B:

The module consists of two identical triggered pulse generators. They produce fast NIM pulses with adjustable width from 50 ns to 10 s and are retriggerable before the end of the output signal. The END-MARKER, a short output pulse at the end of the timing cycle, can be used to delay signals coming from other units or it can provide a self-running rate generator that can be started and stopped at will. By cascading the two sections of the module, a pulse generator with an independent adjustable rate and width can be obtained [20].

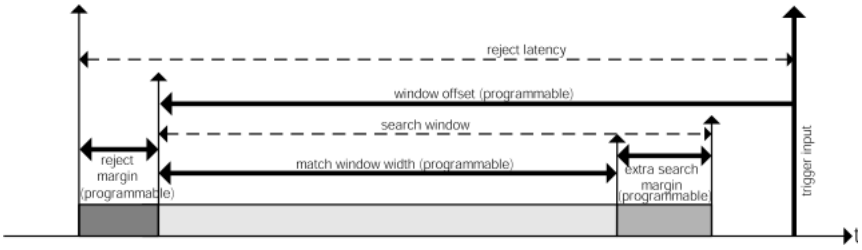

Figure 4.6 – Trigger matching mode timing diagram [19]

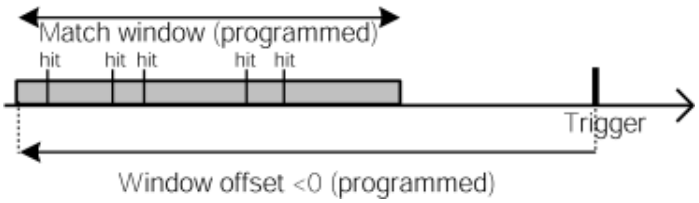

Figure 4.7 – Trigger matching window preceding the trigger arrival [19]

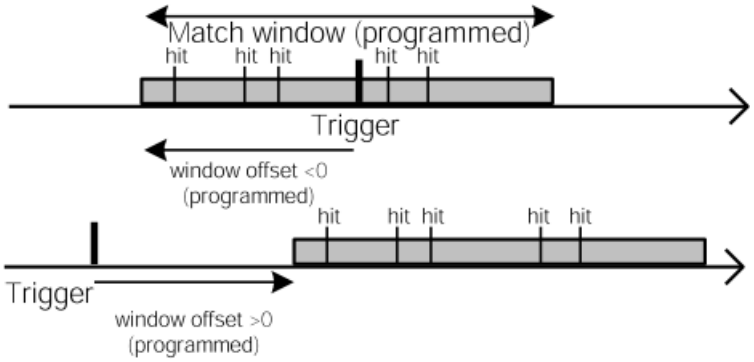

Figure 4.8 – Trigger matching window "staddling" or delayed with respect to the trigger [19]

The CAEN N145 counter:

The unit is a double NIM module that includes 4 independent 8-digit up-counters. The counters can have different operating modes and can be variously interconnected. All control and output signals are standard NIM and the maximum input frequency is 80 MHz, whereas the minimum pulse width is 8 ns [21].

The CAEN double manual programmable logic unit:

The unit consists in a module housing 2 independent logical tables with 4 input and 4 output channels each. The two sections can be programmed independently, activating one or more output channels when one or more input signals are present. It allows, for instance, to identify a coincidence among the signals in the input channels.

4.2 Preliminary Measurements

In section 4.1 we have mentioned the several scopes in which the arch could be useful, however, a preliminary calibration is necessary. The light emitted from the scintillator material travels through the fibers to reach the PMs at the end of them, therefore an accurate measurement of the speed of light in the medium is capital. The efficiency of each detector depends on the applied voltage and it has to be measured in order to know the best voltage to apply. Furthermore, to understand the experimental results, it is very important to know the actual detector efficiency.

4.2.1 Calibration

The aim of this first measurement is to determine the speed of light in the fibers. On the arch there are 16 blue LEDs, however we used only the first 9 LEDs and their positions are reported in table 4.3.

In figure 4.9 a schematic representation of the arch and LEDs is given, in figure 4.10 is depicted the panel which control the LEDs and PMs of the arch.

Using the NIM timing unit we generate a 20 Hz signal, which allows us to select and flash each LED separately at constant frequency. The LED's light is therefore collected by the WLS fibers and routed to PM1 and PM2 at the end of the ribbon. Sending the signals to the NIM modules we can analyze them and in particular, with the TDC module we can measure the difference in time between the arrival of the signals coming from PM1 and PM2, in coincidence with the pulse sent to the LED. Since the space difference between the position of the led and PM1 and PM2 is well known, it is possible to deduce the velocity of light in the medium. Figure 4.11 shows the obtained results.

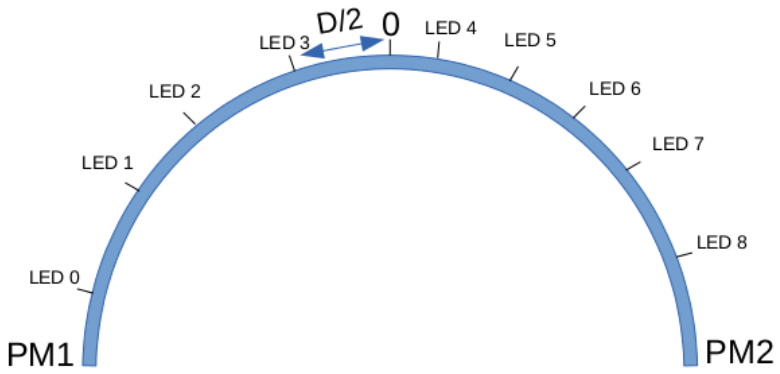

Figure 4.9 – Schematic representation of the distance between the LEDs and PM1 and PM2. D is the length difference between the distance of the LED from PM1 and PM2.

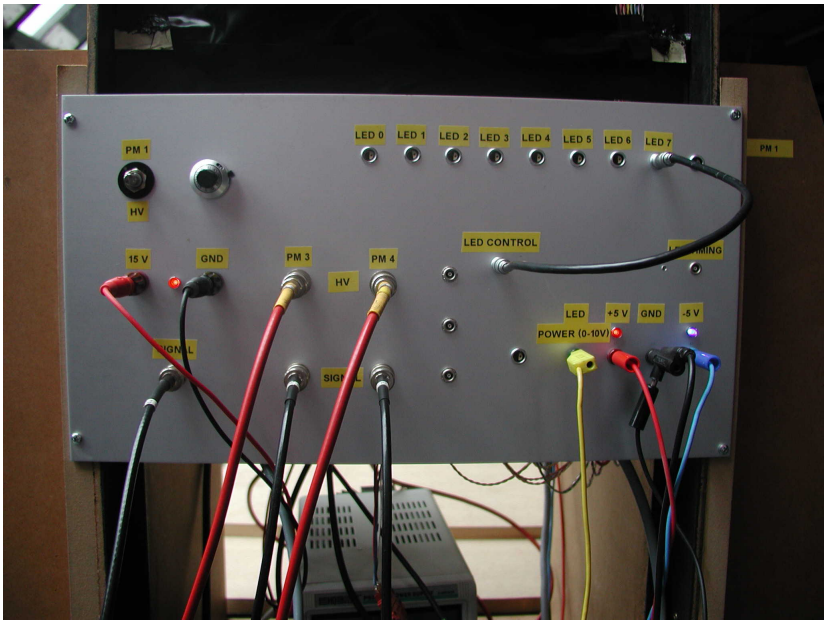

Figure 4.10 – The pannel on the arch. The LEDs connectors, the high voltage connectors and the signal cables are shown.

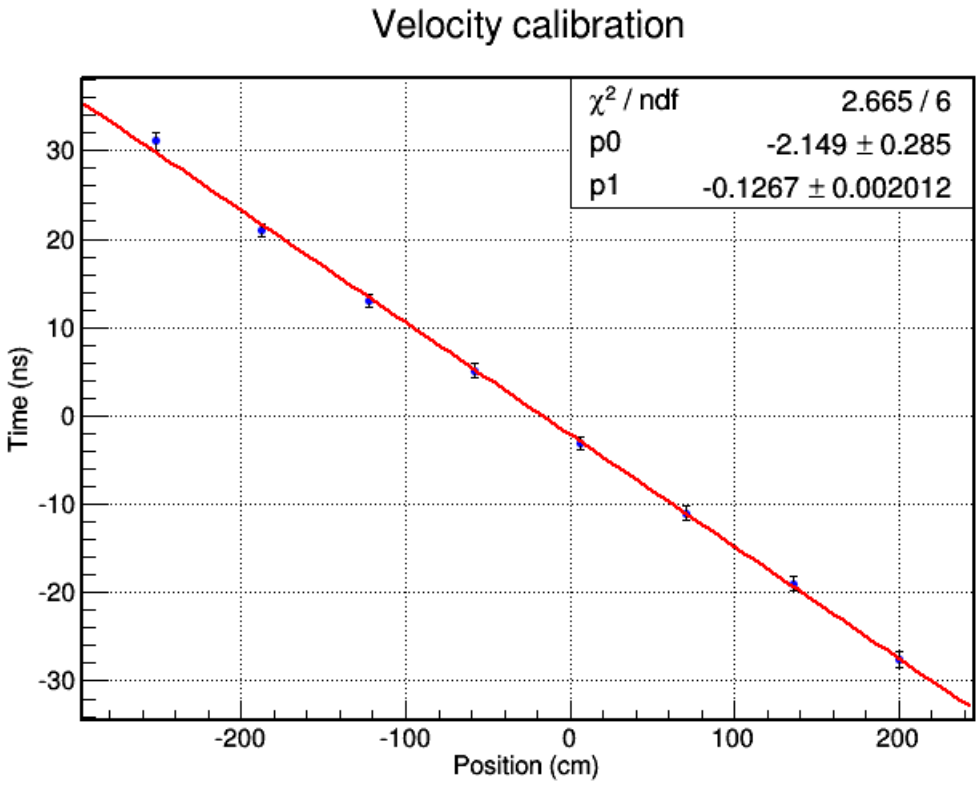

Figure 4.11 – Linear relationship between the positions of the LEDs on the arch and the time difference required by the light to reach PM1 and PM2.

	Position from the top (260.3 cm)
LED 0	-252.1 cm
LED 1	-187.3 cm
LED 2	-122.8 cm
LED 3	-58.1 cm
LED 4	6.4 cm
LED 5	71 cm
LED 6	135.8 cm
LED 7	200.2 cm
LED 8	252.3 cm

Table 4.3 – LEDs positions from the top of the Arch, measured around the circumference

4.2.1.1 Electronic components

Using the dual timer CAEN N93B, we generate the signal allowing LEDs to pulse, as mentioned in the previous section. The NIM modules require digital signals, therefore the analog signal coming from PM1 and PM2 has to be sent to a discriminator first, to be converted in a digital one. A schematic view of the electronics set-up is depicted in figure 4.12 .

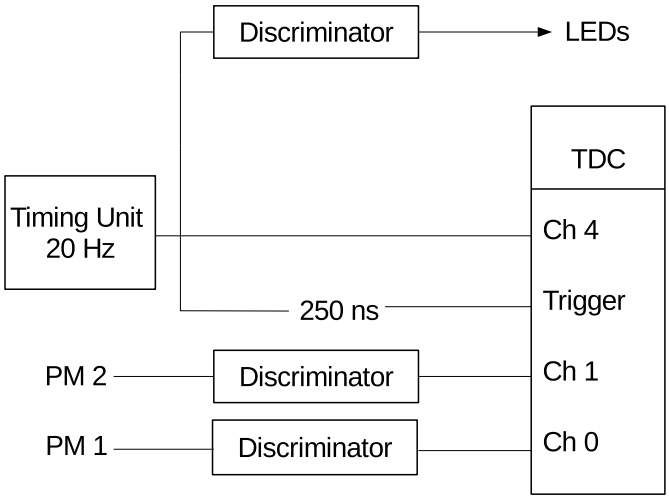

Figure 4.12 – Electronics set-up for the calibration test, schematic view.

PM1 and PM2 have a very low noise level, accordingly the threshold can be set between -2 mV and -3 mV. Afterwards the signals from PM1 and PM2 enter the TDC in two different channels. Two other channels are dedicated to the timing unit pulse and the same pulse delayed of 250 ns. This delay is necessary to observe the coincidence between the flash of the LED and the signal coming from PM1 and PM2. Indeed we have to account for the time required to pulse the LED, for the time needed by the light to travel along the WLS and to get to PM1 or PM2 and eventually by the signal to reach the TDC module. In order to achieve this coincidence, we use *LEMO* cables having an appropriate length to connect the various devices. For completeness table 4.4 summarizes all the delays after time adjustment. .

The TDC module interfaces with a computer where a LABVIEW program allows collecting data and performing statistical analysis. Starting from these data we deduced the time difference between the hits reported by PM1 and PM2 , hence the velocity of light in the medium and we calibrated the arch. In the following section we present the obtained results.

Cable	Time (ns)
Cable 74	41,8
Cable 75	41,8
Cable 81	50
Cable 82	50,4
PM1	7,3
PM2	7,3
PM3	2,8
PM4	2,8
Cable 74 + PM3	44,6
Cable 75 + PM4	44,6
Cable 81 + PM1	57,3
Cable 82 + PM2	57,7
Cable 61 (led t)	51
Cable 62 (led t)	51
Cable 55 (PM5)	67,2

Table 4.4 – Delays of the cables in ns

4.2.1.2 Velocity of light in the WLS fibers

Starting from data collected with the TDC module, one considers the linear relationship between time and distance covered by the light on the arch, as shown in figure 4.11.

The speed of light in the fibers can be immediately deduced from the previous graph, provided that the p1 coefficient is divided by a factor of 2. In fact, the space difference D, between the LED's distance from PM1 and PM2, at the end of the ribbon, is two times the distance of the LED from the origin, at the top of the arch. A schematic representation is given in figure 4.9.

We have hence,

$$\frac{p1}{2} = 0.064 \pm 0.001 \text{ ns/cm}$$
$$v = \frac{1}{0.064} = 15.6 \pm 0.2 \text{ cm/ns}$$

where v is the velocity of light in the WLS fibers.

4.2.2 Efficiency

The detector efficiency relates the amount of particles passing trough the detector to the amount measured by the instrument. It is a relevant feature, which depends on the voltage applied at each detector and in this section we present the different steps involved in its measurement. In section 4.1.2 we have mentioned the detectors at our disposal, the

efficiency measurement concerns the two face to face PMs *Hamammatsu R7400* (PM3 and PM4) as well as PM1 and PM2. As regards PM1 and PM2, an angular dependence analysis has been performed and we considered the total efficiency of PM1 and PM2 as well.

In the present case, it is useful to define the efficiency as follows:

$$\epsilon = \frac{E}{E+I} \tag{4.1}$$

where ϵ is the efficiency, E is the amount of efficient events, namely the events detected by the device under test and I is the amount of the events not detected by the device or, in other words, the inefficient events. The efficiency is always the ratio between the events detected and the total amount of events, but the latter is expressed as the sum of efficient events and inefficient events.

Placing the two plastic scintillators in the apposite stand in the middle of the arch, as mentioned in section 4.1.2, we have three PMs in the middle (PM3, PM4 and PM5), and two PMs at the end of the ribbon (PM1 and PM2).

To measure the efficiency of PM3 as a function of voltage, for instance, we consider the coincidences between the signals coming from PM3, PM4 and PM5 and they constitute the amount of efficient events. Then we count the coincidences between the signals coming from PM4 and PM5, they constitute the amount of total events, efficient and inefficient. We can write the efficiency as follows:

$$\epsilon_{PM3} = \frac{E}{E+I} = \frac{S_{PM3} \bullet S_{PM4} \bullet S_{PM5}}{S_{PM4} \bullet S_{PM5}} \tag{4.2}$$

where S_{PM} is a signal coming from the PM and the $\bullet$ is a symbol which indicates the logical conjunction AND.

4.2.2.1 Electronic components

Using the CAEN double manual programmable logic unit, it is possible to easily satisfy the coincidence requirements of eq. (4.2), in order to measure the amount of efficient and inefficient events.

As already mentioned, each signals coming from a PM has to enter the discriminator first. We used the low threshold CAEN N417 discriminator, the two channels dedicated to PM1 and PM2 have been set on a very low threshold of -3mV. For channels reserved to PM3, PM4 and PM5, a much higher threshold is necessary, indeed they have more relevant noise level than PM1 and PM2.

The quad scaler and preset counter-timer N145 allows counting the amount of events coming from several channels and permits to realize tests over many hours.

Volts	$3 \bullet 4 \bullet 5$	$4 \bullet 5$	**Efficiency**
600	1069	2	0.002 ± 0.001
650	1050	11	0.010 ± 0.003
700	1006	90	0.089 ± 0.009
750	1052	315	0.30 ± 0.01
800	1038	756	0.73 ± 0.01
850	1027	954	0.929 ± 0.008
900	1032	1010	0.979 ± 0.004
1000	1098	1094	0.996 ± 0.002
1100	1048	1047	1.000 ± 0.001

Table 4.5 – In this table are reported: the voltage (Volts) applied on PM3, the amount of collected events and the efficiency. $3 \bullet 4 \bullet 5$ is the coincidence between signals coming from PM3, PM4 and PM5 (number of efficient events), $4 \bullet 5$ is the coincidence between signals coming from PM4 and PM5 (number of total events).

4.2.3 Efficiency Measurements of PM3 and PM4

In section 4.2.2 we gave an expression for the efficiency of PM3, eq. 4.2. By the same token we can express the efficiency for PM3 and PM4:

$$\epsilon_{PM3} = \frac{E}{E+I} = \frac{S_{PM3} \bullet S_{PM4} \bullet S_{PM5}}{S_{PM4} \bullet S_{PM5}} \tag{4.3}$$

$$\epsilon_{PM4} = \frac{E}{E+I} = \frac{S_{PM3} \bullet S_{PM4} \bullet S_{PM3}}{S_{PM3} \bullet S_{PM5}} \tag{4.4}$$

During this measurement, the moveable detector (sc-top) has been placed in the central stand over PM3 and PM4. In order to measure how the efficiency of PM3 depends on the difference of potential applied, a voltage of 900 V has been applied on PM4 and PM5, on the other hand an increasing voltage, between 600 V and 1100V, has been applied on PM3. The exact values are reported in table 4.5.

The same procedure has been followed to measure the efficiency of PM4, but this time we varied the voltage applied on PM4 and we provided a constant voltage of 900 V on PM3 and PM5. The results are reported in table 4.6 and figure 4.14.

In figures 4.13 and 4.14, the efficiency is plotted as a function of the high voltage. The characteristic efficiency-voltage dependence is well depicted and in particular it is apparent the existence of an efficiency plateau starting around 900 V. At 600 V the tension is too low and the detector can not work correctly, increasing the voltage we achieve a higher efficiency. At 900 V we reach a good efficiency of 0.979 ± 0.004, providing higher voltages on PM3 we can increase the detector efficiency but, at the same time, we in-

Volts	$3 \bullet 4 \bullet 5$	$3 \bullet 3 \bullet 5$	**Efficiency**
600	1093	8	0.007 ± 0.003
650	1024	30	0.029 ± 0.005
700	1080	156	0.14 ± 0.01
750	1090	504	0.46 ± 0.02
800	1139	916	0.80 ± 0.01
850	1108	1043	0.941 ± 0.007
900	1188	1153	0.971 ± 0.005

Table 4.6 – In this table are reported: the voltage (Volts) applied on PM4, the amount of collected events. $3 \bullet 4 \bullet 5$ are the coincidence between signals coming from PM3, PM4 and PM5 (number of efficient events), $3 \bullet 3 \bullet 5$ are the coincidence between signals coming from PM3 and PM5 (number of total events).

crease the background noise.

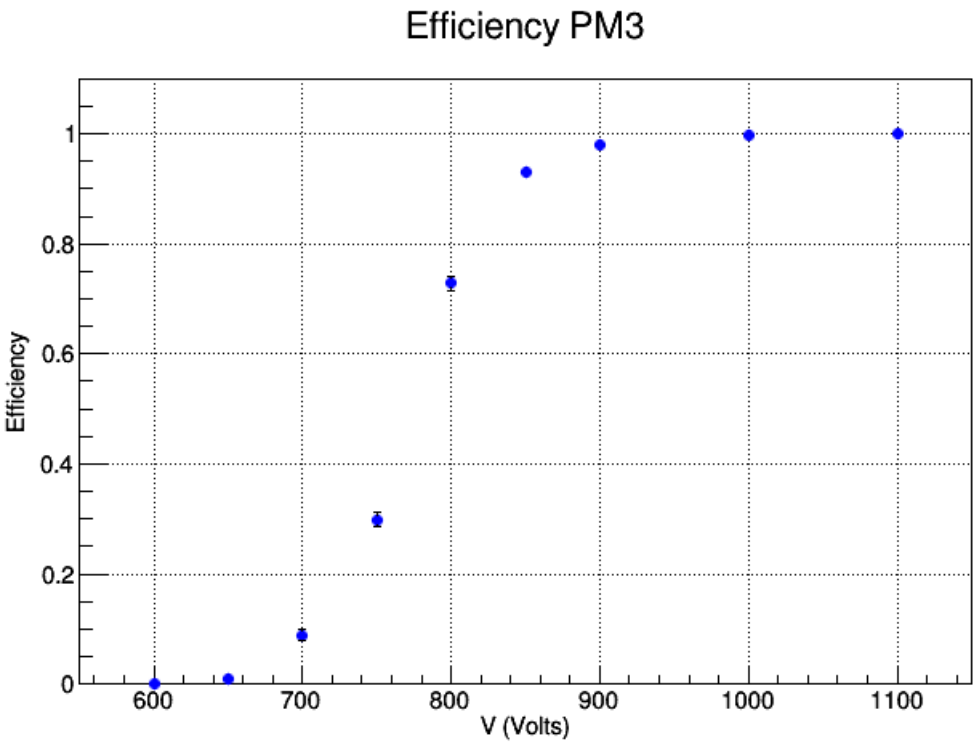

Figure 4.13 – Efficiency of PM3 against different voltage values (V). The efficiency plateau is observed at 900 V.

A way to measure the error on the efficiency values is to assume that the efficient

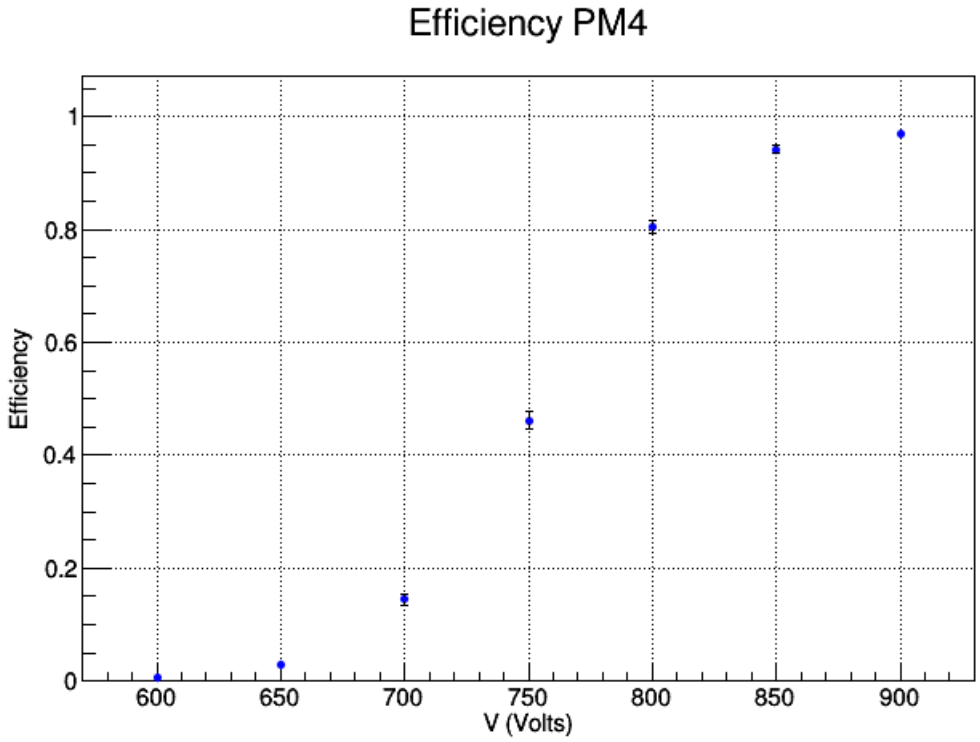

Figure 4.14 – Efficiency of PM4 against different voltage values (V). The efficiency plateau is observed around 900 V.

events E is a binomial variable. In this case the expression of the standard deviation(σ) is well known:

$$\sigma_E = \sqrt{np(1-p)} = \sqrt{(E+I)\epsilon(1-\epsilon)} = \sqrt{N\epsilon(1-\epsilon)} \tag{4.5}$$

In the last expression the number of trials n is replaced by the amount of efficient and inefficient events, namely the total amount of events N passing through the detector and the probability of success, denoted by p, is replaced by the efficiency ϵ. This is a very suitable definition and standard error for efficiency is straight derived from the propagation of uncertainty:

$$\sigma_\epsilon = \frac{1}{N}\sigma_E = \frac{1}{N}\sqrt{N\epsilon(1-\epsilon)} = \sqrt{\frac{\epsilon(1-\epsilon)}{N}} \tag{4.6}$$

There is another way to calculate the efficiency error, we can also assume that the process follows a Poisson distribution, in that case we can assume the standard error of E and I as $\sqrt{E}$ and $\sqrt{I}$. The usual propagation of the uncertainty gives:

$$\begin{aligned}\sigma_\epsilon &= \sqrt{\left(\frac{\partial\epsilon}{\partial E}\sigma_E\right)^2 + \left(\frac{\partial\epsilon}{\partial I}\sigma_I\right)^2} \\ &= \sqrt{\frac{I^2E}{(E+I)^4} + \frac{E^2I}{(E+I)^4}} = \sqrt{\frac{IE}{(E+I)^3}} \\ &= \sqrt{\frac{E}{E+I}\frac{N-E}{(E+I)^2}} = \sqrt{\epsilon\left(\frac{1-\epsilon}{N}\right)}\end{aligned} \tag{4.7}$$

and this is the same expression found in equation 4.6.

4.2.4 Efficiency Measurements of PM1 and PM2

The two photomultipliers, PM1 and PM2, are located at the opposite end of the ribbon which covers the arch. Therefore, the study of their efficiency as function of the angle, is relevant. We fixed the moveable scintillator sc-top, readout with PM5, on the arch's structure, centered on one of the LED's position. A coincidence between an event occurred in PM5 and the two central modules (PM3 and PM4), points out that the particle passed along the arch radius. In this way we can deduce the angle of the cosmic muon that generated the signal. Changing the position of the PM5 on the arch, we can test the efficiency of PM1 and PM2 in different regions of the arch and thus, for different zenith angles.

As expected, the efficiency of the two PMs are angle dependent. The efficiency of one of the two PMs is greater when the muon hits the arch in the corresponding quarter of circumference and in figure 4.15 the efficiency has been plotted against the position on the arch.

In section 4.2.3 we estimated the uncertainty on the efficiency measurements of PM3 and PM4, by the same token we can measure the uncertainty on the efficiency of PM1 and PM2. We selected the muons which hit the arch with a certain angle, to realize this selection we employed the detector sc-top placed on the arch. We accounted for the uncertainty on the position: we considered the surface of the plastic scintillator in use, as reported in table 4.2 its dimensions are 21 cm $\times$ 21 cm, assuming a uniform distribution, for the detector spatial resolution we have:

$$\sigma_d = \frac{D}{\sqrt{12}} = \frac{21cm}{\sqrt{12}} \tag{4.8}$$

where D is the detector width and the factor $\sqrt{12}$ derives from the variance of an uniform distribution [22].

In this chapter we described the facility used to perform the measurements with the triple-GEM prototype in the ULB laboratory. In particular we presented the cosmic arch

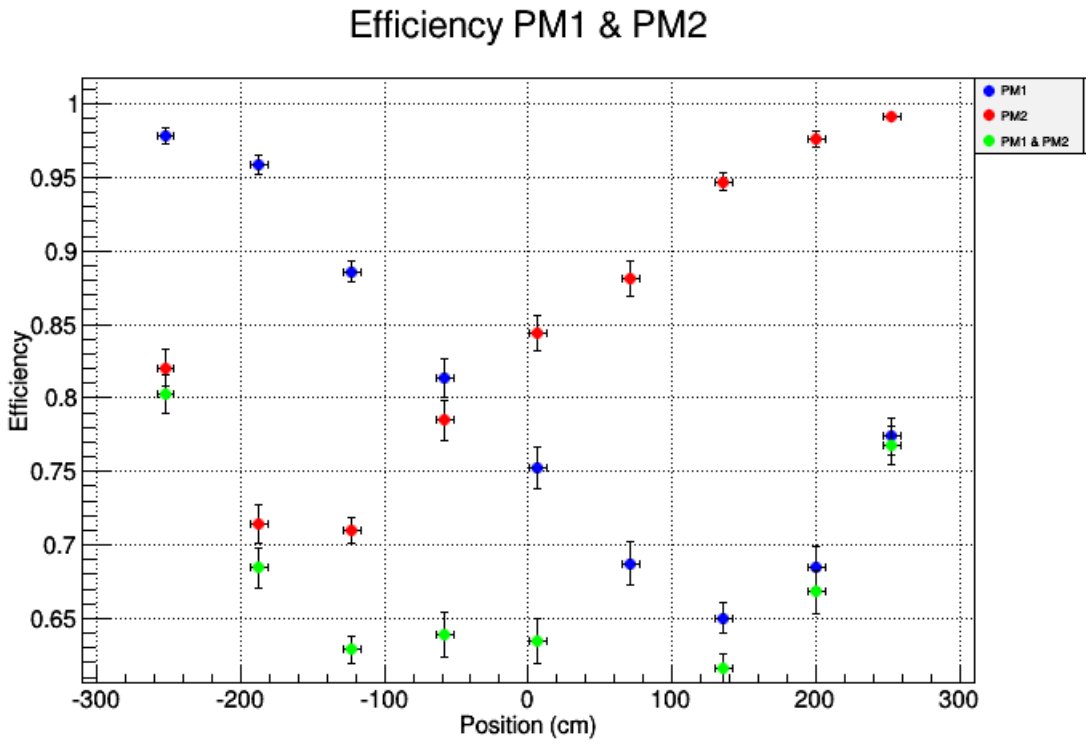

Figure 4.15 – Efficiency of PM1 and PM2 for different zenith angles. The total efficiency is also shown.

and the several electronics modules employed. Moreover we calibrated the cosmic arch and we measured the efficiency of the different detectors at our disposal.

Chapter 5

Characterization of a Small Triple-GEM Detector Prototype

The triple-GEM detectors that will be installed for the upgrade of the CMS forward muon spectrometer are very large. Typical dimensions are $99\ cm \times 22 - 44\ cm$, and therefore relatively expensive, about 5000 EUR. Hence, it is advantageous to characterize the performance of the CMS triple-GEM detectors with small prototypes ($10 \times 10\ cm^2$), they are cheaper and also handier. Small prototypes are useful to test the performance in term of gain, energy resolution, time resolution, efficiency, etc. All these features should be independent on the detector's size.

In this chapter, we will first describe in details the $10 \times 10\ cm^2$ triple-GEM prototype used in this work. In section 5.2 we describe the experimental set-up where the measurements have been performed. Sections 5.3 and 5.4 will present respectively the measurements of the detector gain and efficiency using photons. Finally section 5.5 reports the measurements of the detector efficiency obtained using cosmic muons.

5.1 The $10 \times 10\ cm^2$ Triple-GEM Prototype

In this work, all the measurements have been carried out with a small $10 \times 10\ cm^2$ triple-GEM prototype. Figure 5.1 shows a picture of the triple-GEM prototype used in this work. On the top left and bottom right we can see the gas inlet and outlet respectively. On the bottom left corner we can see the high voltage connector and the high voltage divider, which distributes the voltage to the various electrodes. The divider will be presented in details in section 5.2.4. The detector is sealed with a thin kapton foil surrounded by a thin copper layer for grounding. Figure 5.2 shows a schematic view of the cross-section of the prototype. The readout strips' organization is shown in figure 5.3. There are 2 sets of 256 strips, one along the detector's length and the other along the wide, each set is divided into 2 connectors of 128 channels each.

During the tests we readout only one side of the detector at the time. The strips of the other side are grounded through two 50 Ω resistors as shown on the right side of the detector in figure 5.1.

The prototype has been built with GEM foils manufactured by CERN's printed circuit workshop. They consist in three kapton support of $50\mu m$ with 5 μm copper on each side. The holes have a diameter of 70 μm and a pitch of 140 μm. The prototype has been assembled by the ULB team at CERN in clean room condition, any contact with the active area should be avoided. The main steps of the process are shown in figures 5.4 and 5.5. The readout printed circuit board and the GEM electrodes are assembled first. The latter are mounted on individual frames and they are piled up over the readout plane using insulating pins and spacers [15]. In figure 5.6 we can see the spacing between GEM foils and the plastic spacers. The space of the gaps is reported in table 5.1.

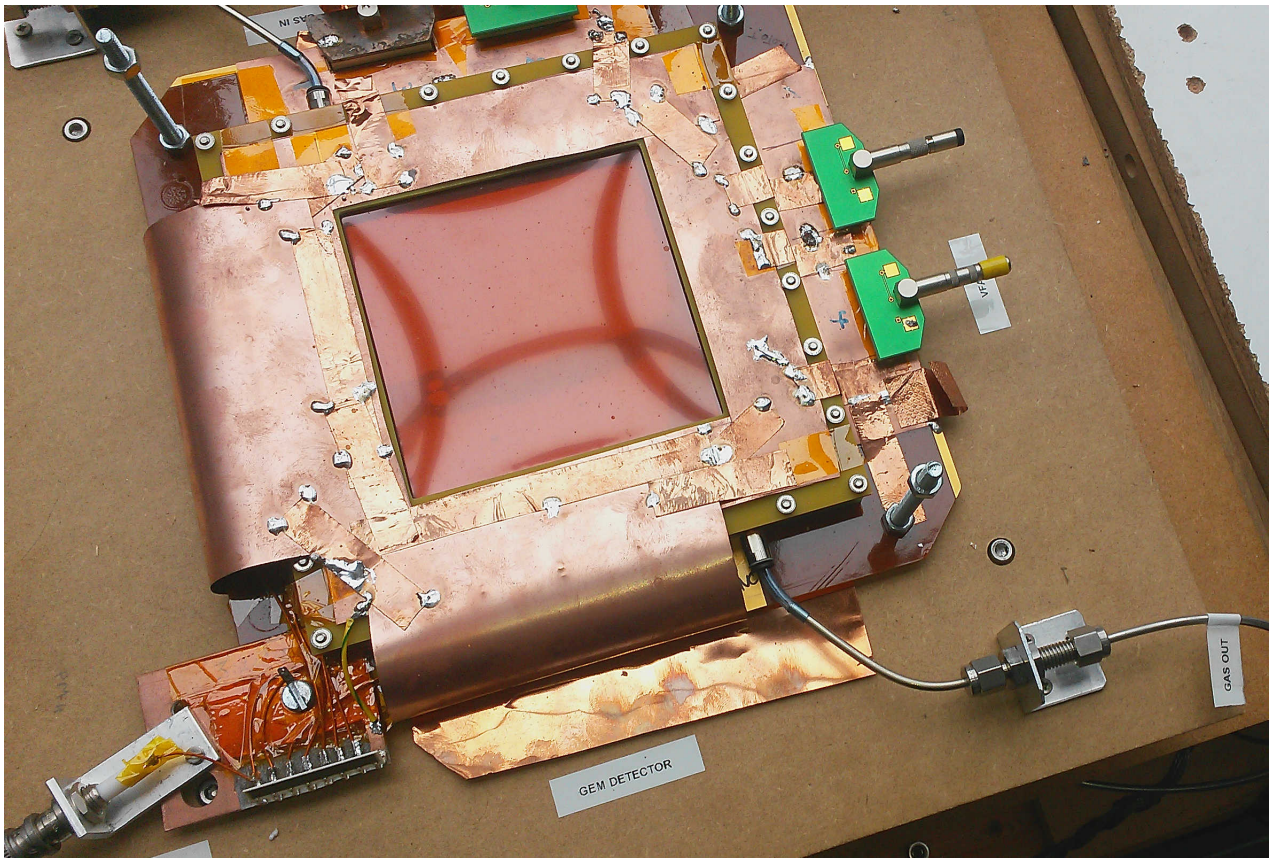

Figure 5.1 – The triple-GEM prototype placed on the central module table. It is connected at the gas inlet, top left on the picture, and the gas outlet bottom right. On the bottom left corner we can see the HV divider.

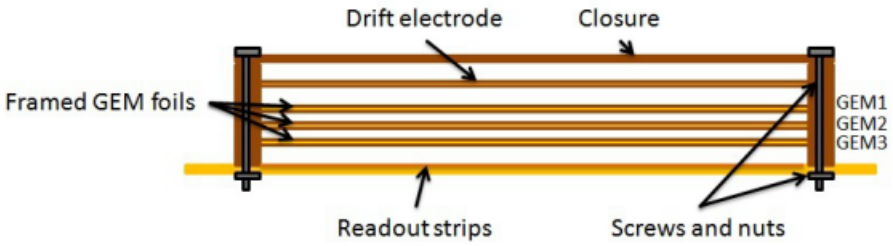

Figure 5.2 – Triple-GEM cross section sketch [23].

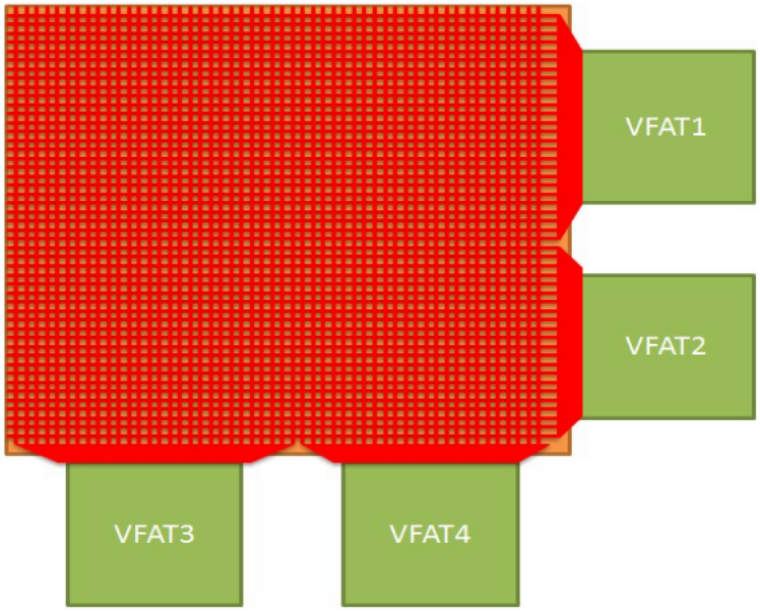

Figure 5.3 – Triple-GEM readout strips [23].

	Prototype $10 \times 10 cm^2$
Drift - GEM1	3 mm
GEM1 - GEM2	2 mm
GEM2 - GEM3	2 mm
GEM3 - Readout	2 mm

Table 5.1 – Gaps between the different GEM foils in the prototype

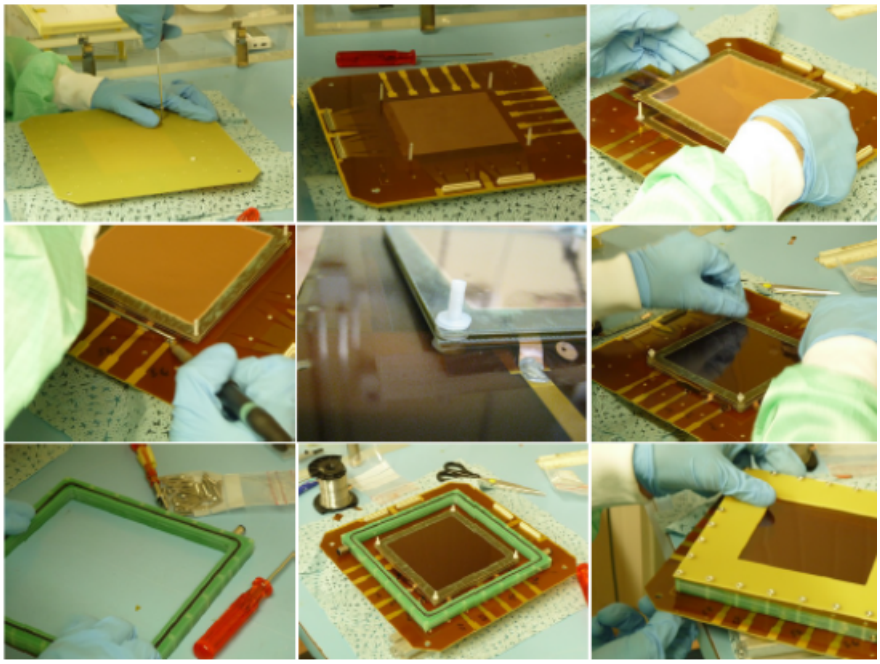

Figure 5.4 – The first steps in triple-GEM prototype's assembly. The readout printed circuit board and the GEM electrodes are combined.

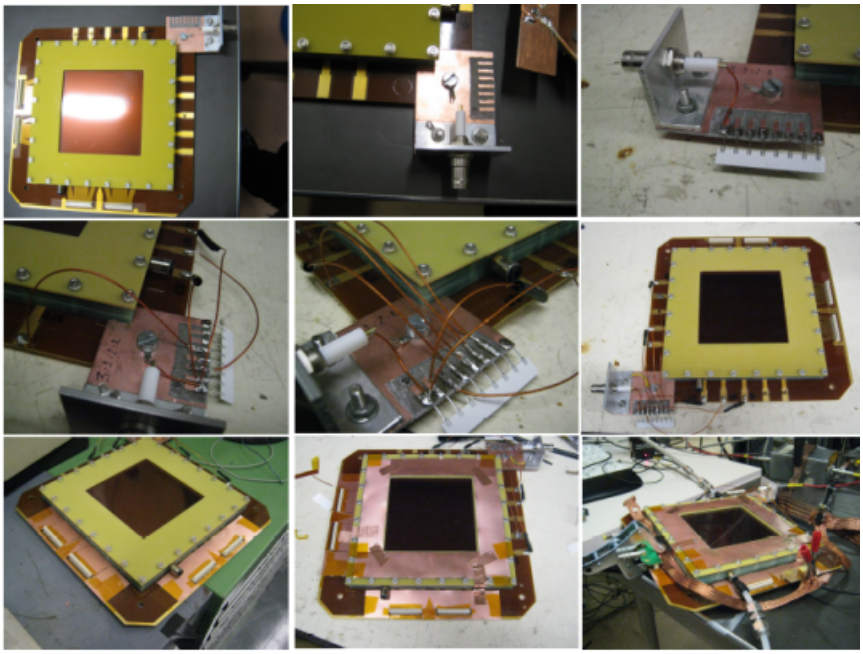

Figure 5.5 – Next steps in triple-GEM prototype's assembly. The HV feedthrough, the gas in/outlet and the roof with the drift plane are connected.

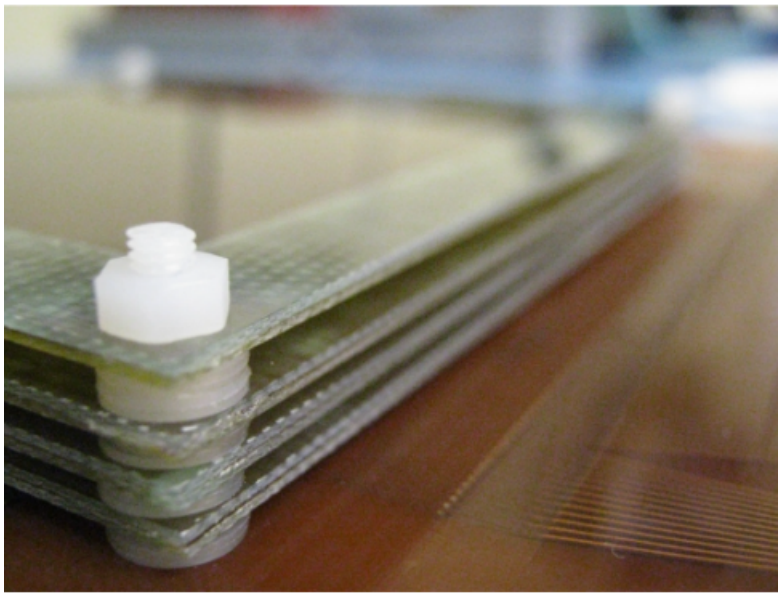

Figure 5.6 – Triple-GEM foils spaced by plastic spacers.

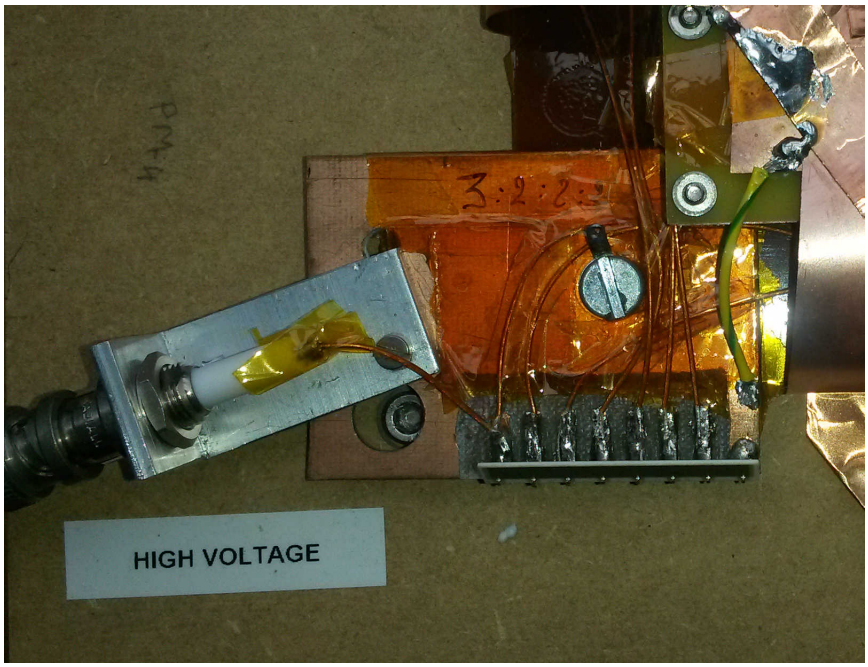

Figure 5.7 – HV divider connected to the prototype triple-GEM detector.

5.2 The Experimental Set-up

The experimental set-up is based on the cosmic muons arch described in chapter 4. In figure 5.8 we can see the small triple-GEM prototype mounted on the table in the middle of the arch. The prototype lies between the central scintillator of the arch, sc-bot (see section 4.1.2), and the movable scintillator, sc-top. A stage has been built to support the movable plastic scintillator as shown in figure 5.9.

Figure 5.8 – The arch setup with the triple-GEM detector placed between the scintillator sc-bot and sc-top.

5.2.1 Signal Amplification

The NIM electronics modules are the same used during the arch's calibration but to read out the faint signals coming from the strips of the triple-GEM , an external amplification process is required. A first amplification is achieved employing an *ORTEC 142B preamplifier*.

The *ORTEC 142B preamplifier* is a charge sensitive preamplifier. The output signal is a fast rise time voltage step ($\approx$ 50 ns) with an exponential return to the baseline in about 75 μs. The preamplifier inverts the polarity of the input signal.

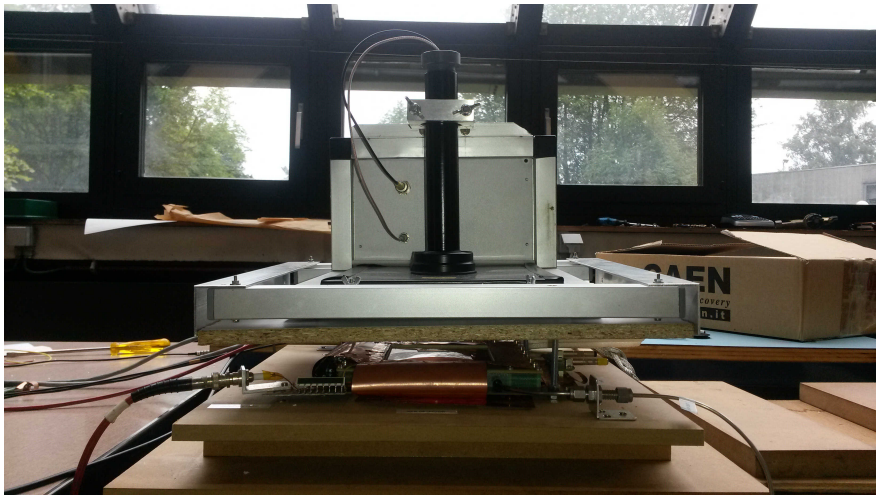

Figure 5.9 – The central modules table at the center of the arch. The bottom scintillator sc-bot is inside the wood box. The triple-GEM prototype is placed between the two plastic scintillators, sc-top and sc-bot.

To improve the signal-to-noise ratio and to produce semi-Gaussian shaped pulse [24], the output signal of the preamplifier enters the shaper *ORTEC 575 amplifier* and eventually enter the *LeCroy 429 Linear Fan-In-Fan-out* and then the discriminator. The readout electronics circuit is shown in figure 5.10

The outgoing signals of the triple-GEM detector have a negative polarity, however, since the preamplifier inverts the polarity of the incoming signals, the output of the preamplifier is a positive signal. The NIM discriminator module accepts only signals with negative polarity, hence, before enter the discriminator the signal's polarity has to be inverted by the Linear Fan-In-Fan-Out.

5.2.2 Digital Logic

In figure 5.11 a typical analog GEM signal and the corresponding digital one are shown. The digital signals produced by the discriminator have an adjustable width but its maximum value is 800 ns. The analog signal provides by the GEM detector, after the preamplification and amplification stage has a typical duration of 2.5 μs, which is much longer than the corresponding digital one. Moreover the GEM signal shows a long tail. In section 4.1.3 we explained how the discriminator works and how the signal is generated over a certain threshold, which in th present case is set to 80 mV. If the analog signal is longer than the digital one the discriminator will crate multiple gates for the same analog signals, generating fake events. In order to avoid this issue, we adopted a more complex electronics setup. In figure 5.12 the electronics diagram is shown.

A way to avoid the multiple gates formation is to open a VETO gate immediately

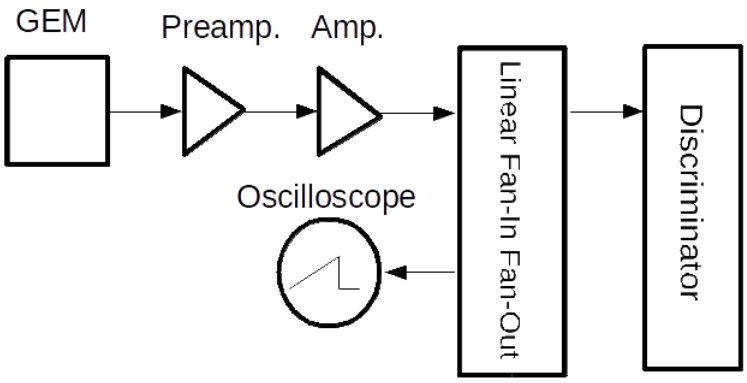

Figure 5.10 – Scheme of the triple-GEM readout electronics.

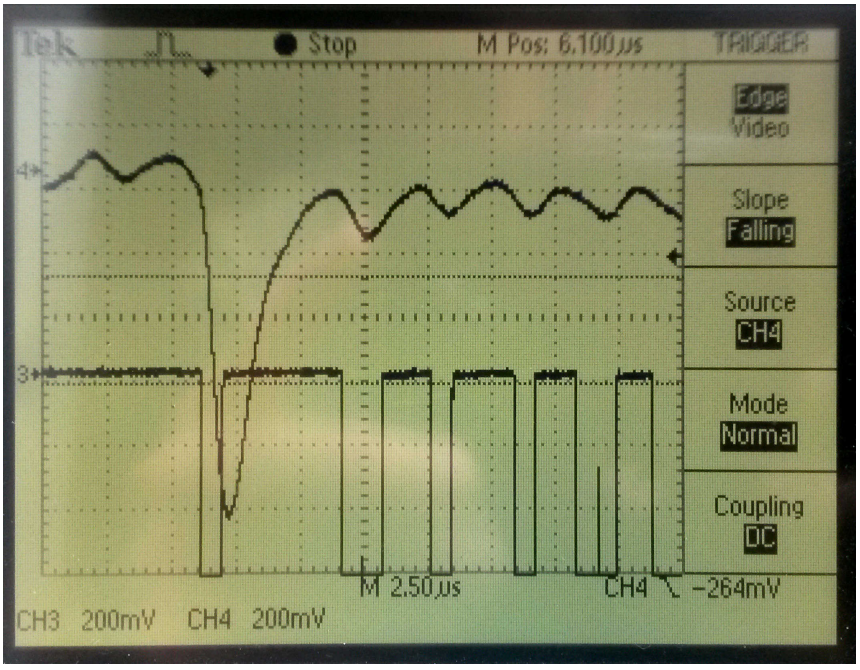

Figure 5.11 – The analog signal for the GEM detector with the corresponding digital one. The threshold is 80 mV, the discriminator opens multiple gates for a single GEM signal.

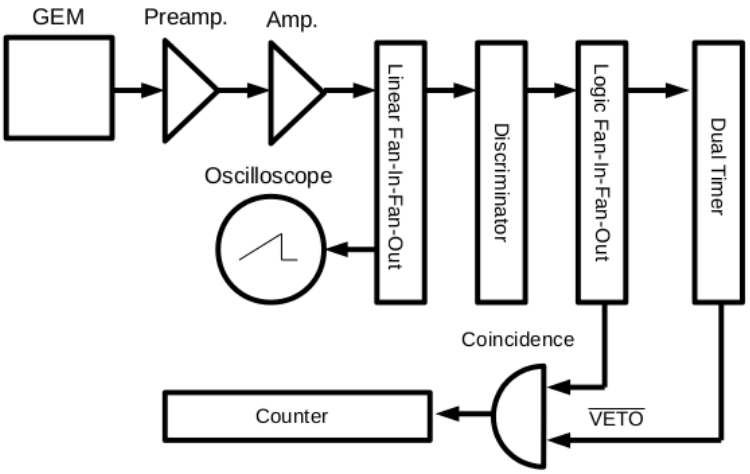

Figure 5.12 – Diagram of the electronics modules used during the measurement of the efficiency. The discriminator: threshold = 80 mV, width = 800 ns.

after the creation of the first signal and, using the logic module, consider other discriminator signals only if there is no VETO in concomitant with them. The VETO's duration must be carefully adjusted, in the present case we decided to set the VETO's duration to 50 μs. On one hand this time lapse allows rejecting every fake signal and on the other hand it is short enough to not compromise the rate measurement.

5.2.3 Gas Mixture

The mixture used during these tests is Ar/CO_2, with 70 % of Ar and 30 % of CO_2. The gas mixture is provided through a gas mixer and the gas flows are controlled by *HORIBA* flow meters [25], monitored remotely over ethernet. Figure 5.13 shows the mentioned flow meters.

5.2.4 High Voltage Supply and High Voltage Divider

We used the C.A.E.N. N470 multichannel high voltage power supply to connect all detectors (GEM, PMs). We provided a voltage from -4000 V to -4900 V to the GEM detector. The resistor divider, shown in figure 5.14, allows us to power all the GEM foils, creating the sought differential of potential between the gaps. Each element of the detector is connected to the divider and the voltage drop depends on the resistor value. It is straightforward to compute the electrical field in the drift and in the transefer regions:

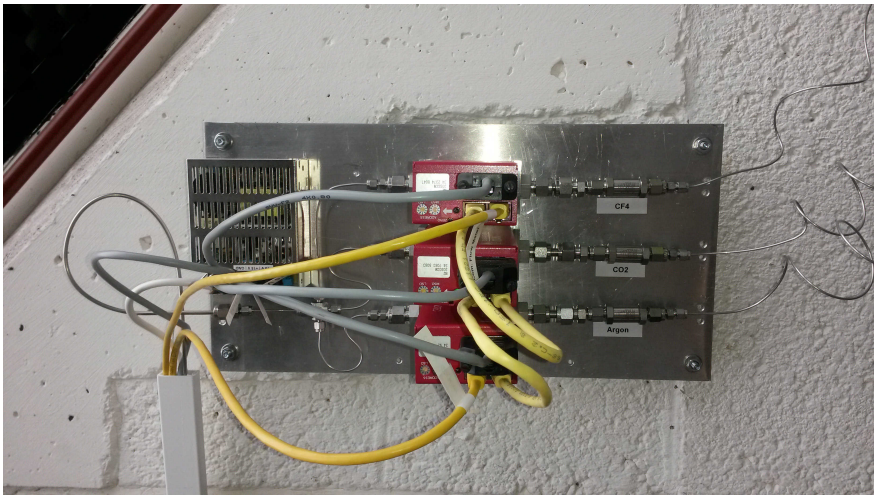

Figure 5.13 – *HORIBA* flow meters monitored remotely over ethernet.

$$E = \frac{IR_{divider}}{\Delta x} \tag{5.1}$$

Using a cable per GEM's element should be a more direct way to provide the correct potential on each element of the triple-GEM detector, however this solution causes a considerable increase of number of cables and it is not feasible.

In addition the voltage provided by the HV power supply passes trough a small HV RC filter before entering the HV GEM's divider, for the following reason. The filter acts as a low-pas filter, absorbing the high frequency signals on the line to provide a stable voltage to the electrodes. The filter's scheme is shown in figure 5.15. It is composed by 3 resistors of 100 $k\Omega$ and 2 capacitance of 2.2 nF.

5.2.5 Grounding and Noise

The first measurements with the triple-GEM prototype were affected by a very high noise level. A way to reduce this inconvenience is to improve the grounding of the whole readout electronics and in particular the preamplifiers. Using copper foils we connected the preamplifier's ground with the NIM electronics ground and we connected the detector to the ground as well. Moreover, to reduce the noise at the input of the preamplifier we have to bring the preamplifier as close as possible to the strips. In our set-up this is only possible using 3 cm long LEMO cables.

The reduction of noise has been an important task of my work and it was capital to allow reading out the GEM signals, in particular fainter signals as the one generated by

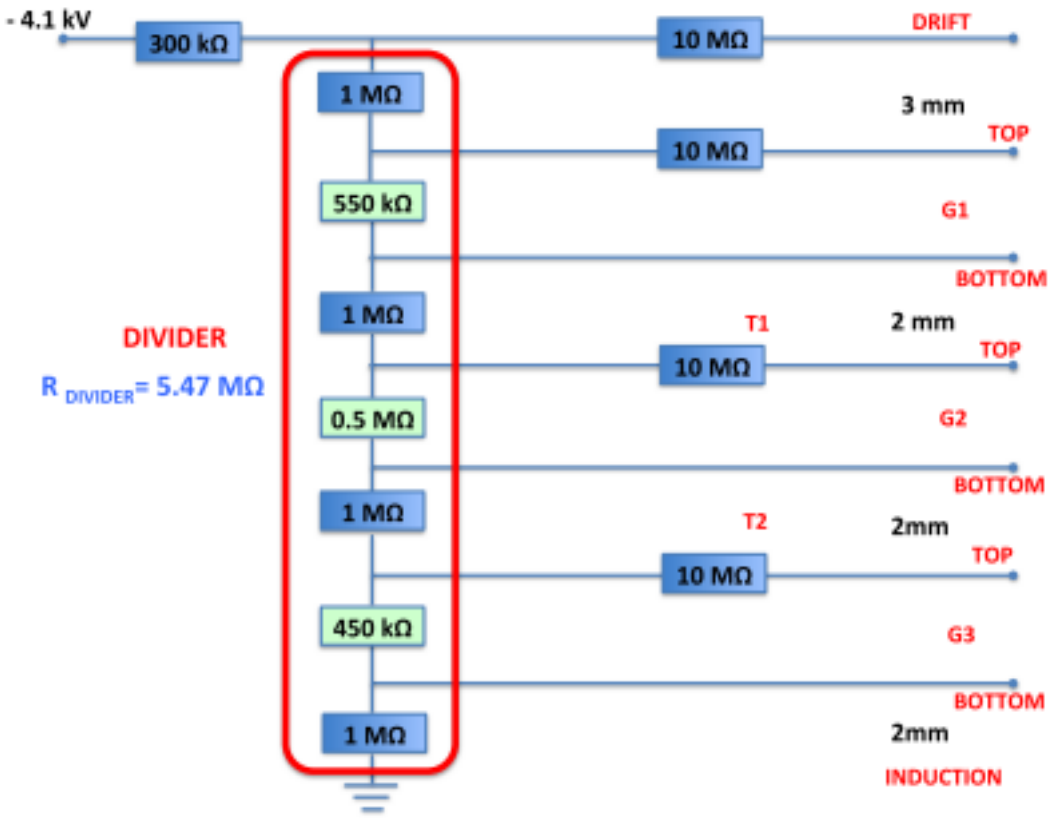

Figure 5.14 – High voltage resistor divider scheme.

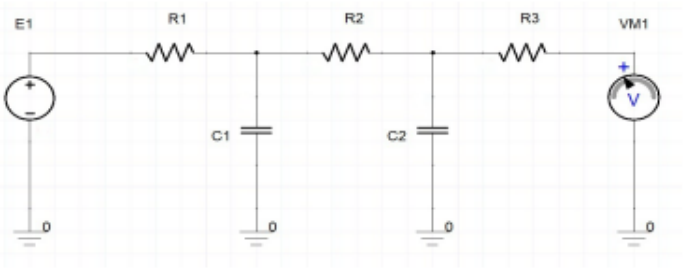

Figure 5.15 – Scheme of the HV filter [23].

cosmic muons. In the future a Faraday cage should be installed in order to shield better the detector from environmental noise.

5.3 Gain Measurements

The effective detector's gain G_{eff} is the ratio between the number of electrons at the end of the triple-GEM amplification process and the number of the primary ones.

$$G_{eff} = \frac{N_{el}}{N_p} \tag{5.2}$$

where N_{el} is the amount of the electrons in the induction gap, which generate the outgoing signal and N_p is the amount of primary electrons, produced in the drift zone by ionization.

In GEM detectors G_{eff} is smaller than gain of the GEMs, due to transparency and the losses of electrons along their drift path inside the GEM holes, see 3.5.1.

5.3.1 Iron-55 Source

To measure the triple-GEM prototype's gain, we should estimate the number of primary electrons generated by an interaction in the drift zone and then measure the total amount of electrons which generate the signal. To this aim it is very useful to use an X-ray source like Iron-55, whose energy spectrum is well known. Moreover the source is easy to control, in particular, it can be moved along the full detector sensitive area. In figure 5.16 is depicted the triple-GEM prototype with the Iron-55 source placed on the top. A metal collimator is used to irradiate only a few strips at the time.

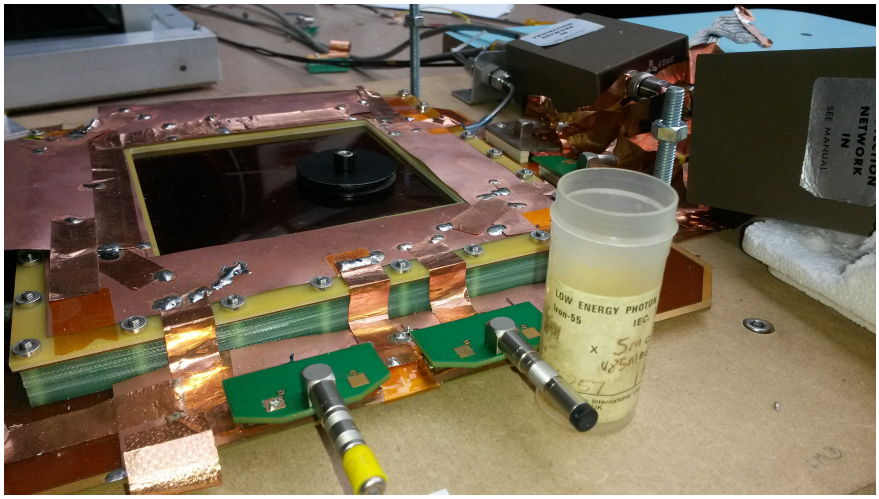

Figure 5.16 – Triple-GEM prototype with the Iron-55 source placed on the top.

The main emission line for the iron-55 source is at 5.9 keV. In most of the cases the whole photon's energy is absorbed and used to produce primary ionization electrons. However in the some cases the photon extracts an electron from the inner K-shell of the

argon and the vacancy is filled by an outer electron, with the emission of another X-Ray photon of 2.9 keV, as mentioned in section 2.1. If this photon escapes from the detector, the corresponding amount of energy is lost and we observe a second peak in the iron-55 spectrum, called escape peak. In figure 5.17 is shown the X-ray absorption spectrum for iron-55 in argon.

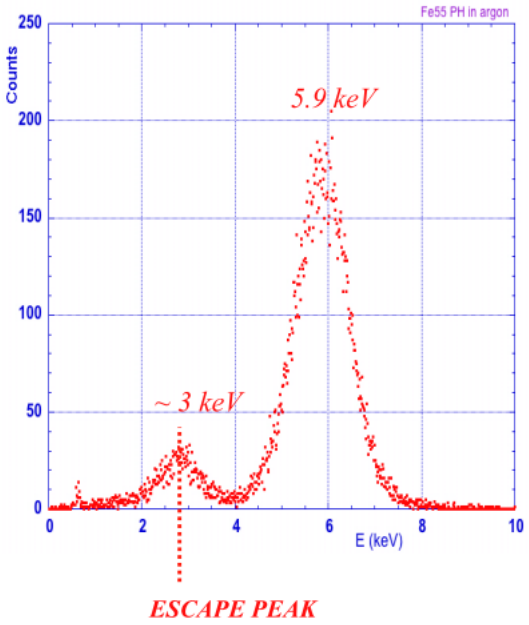

Figure 5.17 – X-ray absorption spectrum for iron-55 in argon.

In section 2.1 we described the ionization process and we introduced the mean ionization energy W, which is the energy necessary to ionize the medium.

All tests on the prototype have been performed with the Ar/CO_2 - 70/30 % gas mixture, hence we have to calculate an average W_γ value for the mixture in use. The Ar and CO_2 W values are reported in table 2.1 and the mean is computed as follows:

$$\frac{1}{W_\gamma} = \frac{\%(Ar)}{W_{Ar}} + \frac{\%(CO_2)}{W_{CO_2}} = \frac{1}{27.8} \tag{5.3}$$

Now we can compute the average number of primary electrons produced by an X-ray photon of 5.9 KeV:

$$N_p = 5.9KeV\frac{1}{W_\gamma} = 212 \tag{5.4}$$

5.3.2 Test Pulse Calibration

In the previous section we estimated the number of primary electrons generated by an iron-55 photon, in the gas mixture. To obtain the detector's gain we have to measure the charge collected by the readout strips.

The charge produced in the induction region is too small to be measured with a common ammeter and, consequently, we can exploit the linear behavior of the preamplifier instead. To achieve this goal, it is capital to calibrate the preamplifier, studying the output voltage as function of the input charge.

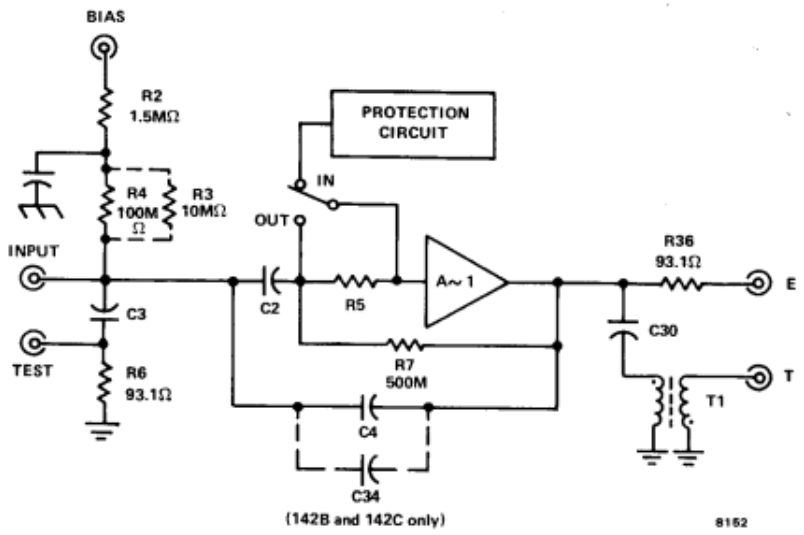

Figure 5.18 – Simplified block diagram of the circuitry in ORTEC 142A, 142B, 142C preamplifiers [26].

On the ORTEC 142B preamplifier, we can find an apposite input test connector which accepts input voltage pulses from a pulse generator. Figure 5.18 shows a simplified diagram of the circuit. C3 is a 2pF capacitor, hence, using an external amplitude generator, we can send a square pulse into the pulse test input connector and we observe the voltage at the output with an oscilloscope. Since we know the capacitance of the internal circuit connected at the pulse test connector, we know the amount of charge which generates the observed output voltage.

Figure 5.19 represents the output voltage as a function of the charge, in number of e^-, sent at the preamplifier input. The charge released by a capacitor simulates the signal coming from the triple-GEM detector and it allows us to employ the linear relationship found in the other way round to measure the charge outgoing the detector. Once we

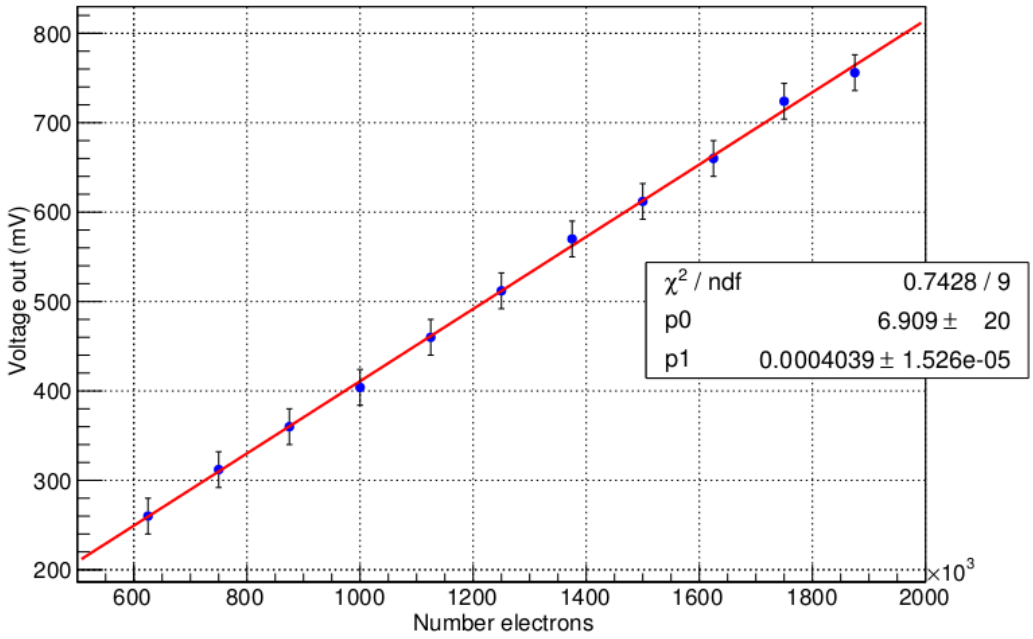

Figure 5.19 – Relationship between the charge at the input test pulse of the preamplifier and the output voltage. The charge depends on the ΔV of the square pulse sent on the internal RC circuit.

know the linear regression coefficient p1 we can measure the voltage on the output of the preamplifier to deduce the charge at its input and finally measure the detector's gain.

5.3.3 Triple-GEM Prototype's Gain

The iron-55 source allows us to measure the gain of the triple-GEM prototype as function of the HV applied. We put the source on the top of the GEM detector and we observed the signals with an oscilloscope. As already mentioned the signals pass trough the preamplifier and the shape amplifier before entering the oscilloscope, see figure 5.12.

On the oscilloscope the signals issued from the 5.9 keV peak are well visible and we can measure their corresponding amplitude. From the amplitude, using the calibration curve of section 5.3.2, and knowing the number of primary electrons released by a 5.9 keV photon, we can measure the G_{eff} of the triple-GEM detector.

In figure 5.20 and 5.21 some results acquired in different temperature and pressure conditions are shown. The triple-GEM detector shows high gains up to 14,000 and it remains very stable, in particular any discharge has been observed.

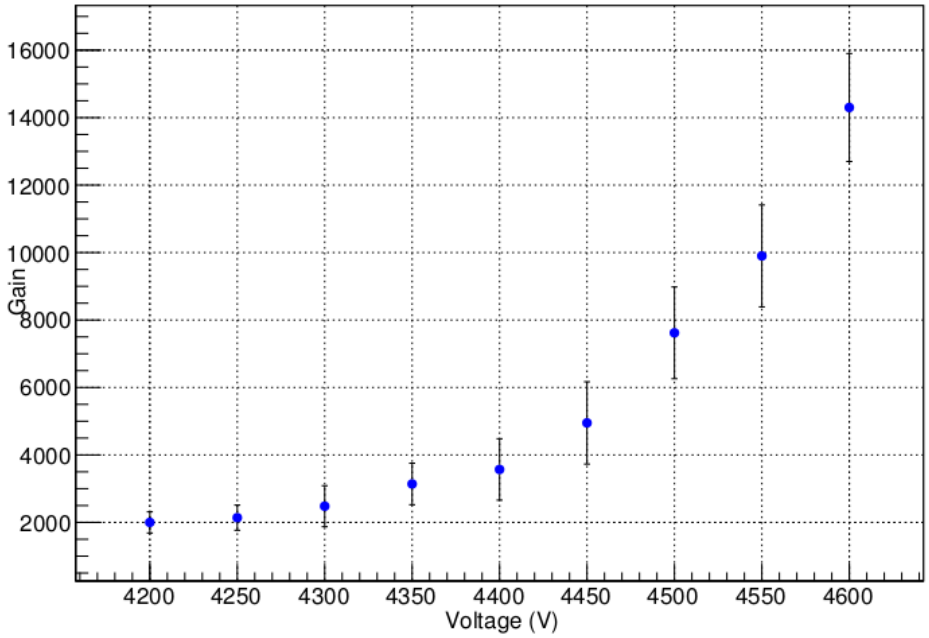

Figure 5.20 – Gain of the triple-GEM prototype. T=21.3 ^oC and Pressure=1020 mb

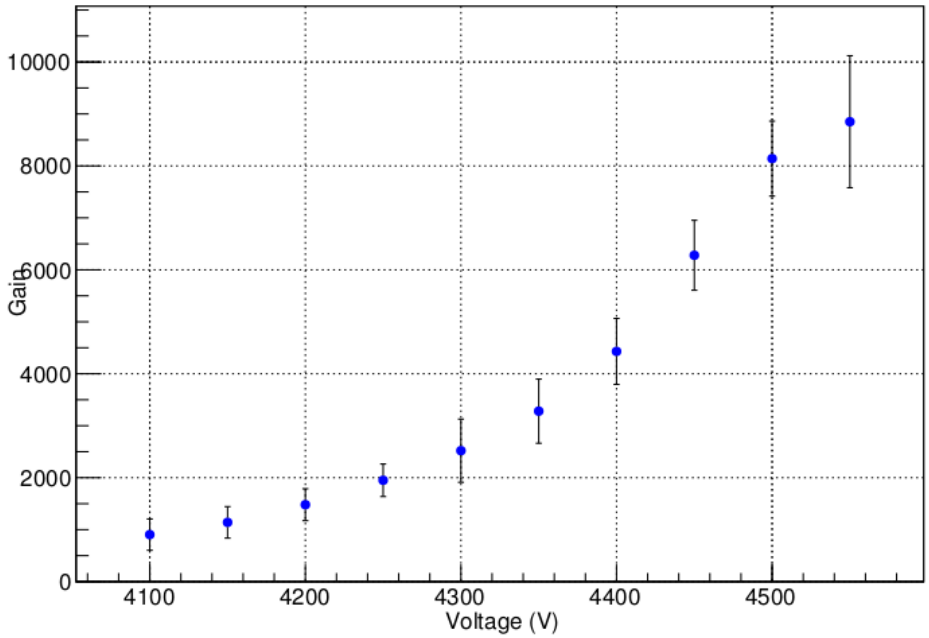

Figure 5.21 – Gain of the triple-GEM protptype. T=22.4 ^oC and Pressure=1010.6 mb

5.4 Efficiency Measurements Using Photons

A relevant measurement during the detector's characterization is to work out at which voltage the detector is fully efficient. A way to achieve this goal is to use the X-ray source in order to observe the rate measured by the detector for several voltages applied. At the beginning, the rate will be less than the real source rate, since the detector is not completely efficient. Once the HV applied allows the detector to be completely efficient, the rate will be constant increasing voltage and therefore we can observe the typical plateau trend of figure 5.22. We can conclude that the prototype begins to be fully efficient around 4500 V for 5.9 keV photons.

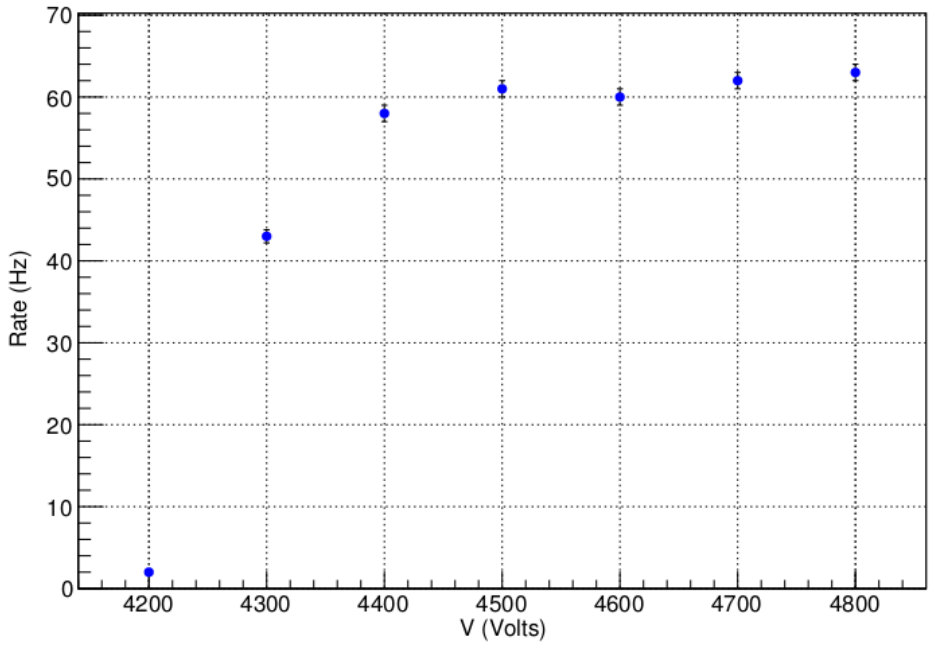

Figure 5.22 – Plateau observed measuring the source's rate with different HV applied on the triple-GEM.

5.5 Efficiency Measurements Using Cosmic Muons

The setup present in the lab allows us to perform efficiency measurements using the cosmic muons. They are produced when cosmic rays collide with nuclei in the Earth's upper atmosphere.

The angular distribution of the cosmic rays varies as $\cos^2\theta$, where θ is the zenith angle, measured with respect to the vertical direction. The angular distribution is caused by two reasons, firstly, the primary cosmic rays are extremely energetic and particles

produced in the same direction as the primary have high momenta and energy. Therefore muons produced along the primary direction have more chances to get the detector before decaying. Secondly, the distance, which muons has to travel to get the detector, increases as function of the angle from the vertical and the probability to decay before reaching the detector increases. Combining the two effects, the approximated expression for the differential flux of cosmic ray muons, per unit of time, per unit of area and per unit of solid angle, reads:

$$\frac{dN}{dAd\Omega dt} \approx I_0 \cos^2\theta \tag{5.5}$$

where θ is the polar angle, $I_0 \approx 0.66\ cm^{-2}sr^{-1}min^{-1}$ at sea level.[27]

Integrating over the solid angle we have an approximation of the rate of cosmic rays passing through an horizontal unit area:

$$\int_{\Omega/2} 0.66\ \cos^3\theta\, d\Omega = 1.04\ cm^{-2}min^{-1} \tag{5.6}$$

5.5.1 The triple-GEM Prototype Efficiency

The efficiency measurement of the triple-GEM prototype follows the general concepts presented in in section 4.2.2. We used sc-bot, sc-top and the GEM detector placed between the scintillators as in figure 5.23. The coincidence of signals from the PMs constitute the trigger signal to measure the triple-GEM efficiency.

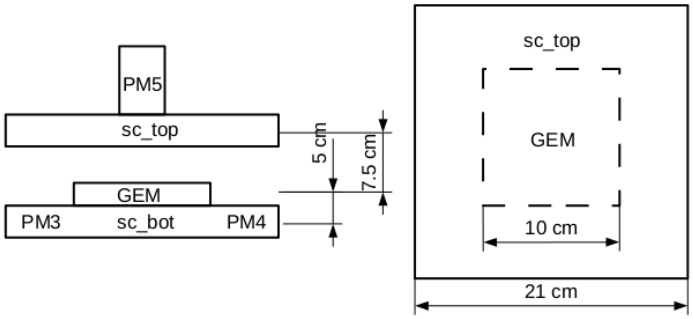

Figure 5.23 – Central modules' scheme, PM3 and PM4 read the same plastic scintillator (sc-bot). The GEM is in the middle of the table and sc-top is over other detectors.

5.5.1.1 Electronic components

In order to measure the triple-GEM's efficiency, we employed the NIM modules in the same way as in section 4.2.2.1. However we add the dual timer CAEN N93B because of

	Width	Threshold
PM3	7.5 μs	30 mV
PM4	7.5 μs	30 mV
PM5	7.5 μs	150 mV
GEM	7.5 μs	80 mV

Table 5.2 – Threshold and width for the discriminator units used for PMs and GEM.

the presence of relevant delay between PMs and GEM's signal, the necessity to enlarge the window's width in order to fit the long triple-GEM signal (2.5 μs) and creation of a VETO to reduce the probability of fake signals, see 5.2.2.

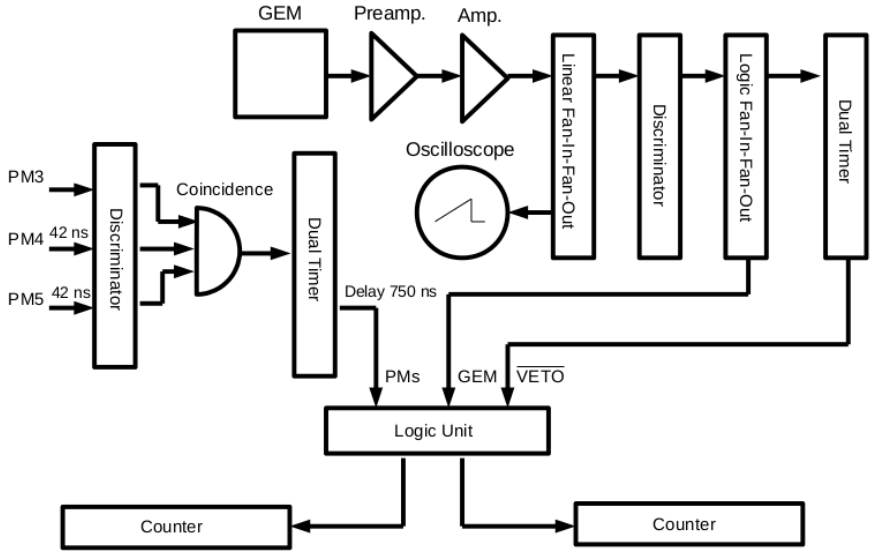

Figure 5.24 – Diagram of the electronics modules used during the measurement of the efficiency.

A diagram of the electronic components is given in figure 5.24 and in table 5.2 we give the values of threshold and width of the discriminator units.

First of all, we have to find the coincidence between the three signals generated by PM3, PM4 and PM5, when an atmospheric muon pass through them. There are two different models of PMs in use and they have different time responses, moreover the cables connecting them to the NIM modules have not the same length. PM5 has therefore a relatively small delay of about 42 ns, in comparison with PM3 and PM4, see figure 5.25. Using two long cables, we delay the signals coming from those PMs and remove the delay. To get the coincidence between all three detectors, we use one of the two logic units.

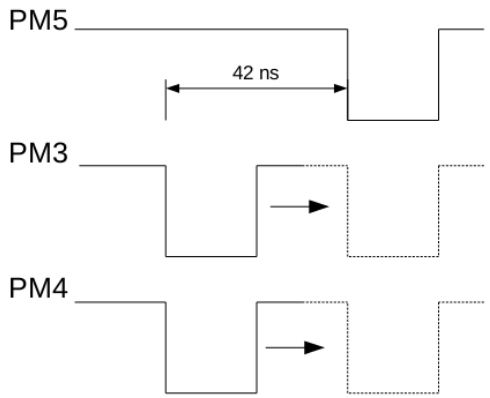

Figure 5.25 – At the beginning there is no coincidence between PM5, PM3 and PM4(continuous lines). After delaying PM3 and PM4 with long cables, the three signals are in coincidence (dashed lines).

Also the GEM signal has a delay, but in this case it is much longer, that is about 750 ns. Such important delay is due to the electronics, the triple-GEM signal has to pass through the preamplifier and the shaper amplifier before reaching the discriminator. In order to get the coincidence between PMs and GEM detector, we have to delay the output of the previous logic unit, namely the signal generated by a coincidence between the PMs. In this case we can not simply use a longer LEMO cable, because the delay needed is too long. Hence we use the dual timer to delay that signal and we eventually entered the other logic unit.

Observing the analog signal coming from the triple-GEM detector with the oscilloscope we can select the appropriate threshold and width, respectively 80 mV and 7.5 μs. Afterwards the signal coming from the discriminator enters the Logic Fan-In-Fan-Out which duplicates it. One of the two outputs allows us to realize the VETO and the other one enters directly the logic unit.

The VETO is opened immediately after the end of the discriminator signal from GEM, the delay necessary to that is achieved using the dual timer. The signals is also enlarged to last enough to cover the whole GEM's analog signal before enter the logic unit.

At this stage we can satisfy the coincidence requirements and measure the GEM's efficiency using two counters.

5.5.1.2 The geometrical acceptance of the detectors

Since the triple-GEM detector is placed between two plastic scintillators as discussed in section 5.5.1, we have to take into account the detectors' geometrical acceptance.

The geometrical acceptance accounts for all geometrical effects that may lead muons to miss the detector under test. The gap between detectors, for instance, allows some particles hitting one detector but not the others. In the present case we have to consider also the different dimensions of the scintillator and the triple-GEM prototype, see scheme in figure 5.23.

To estimate the geometrical acceptance I wrote a small python code to perform a Monte Carlo simulation. The value of the acceptance ϵ_{Acc} is 0.448 if we take into account only the 2 scintillators of 21 cm with a gap of 12.5 $\pm$ 1 cm. The statistical error on this value is $\pm$ 0.007, whereas the error from the uncertainty on the measurement of gap distance leads to an error on the estimation of $\pm$ 0.03, therefore we have $\epsilon_{Acc} = 0.45 \pm 0.03$. So the 45 $\pm$ 3 % of the muons hit both detectors. If we consider both scintillators and the triple-GEM detector placed between them, as in figure 5.26, we have to compare the rate of muons passing through the scintillators with the rate of muons hitting the scintillators and also the triple-GEM. We get ϵ_{Acc} of 0.39 $\pm$ 0.03, which means that the 39 $\pm$ 3 % of muons which hitted the scintillators, reached also the triple-GEM.

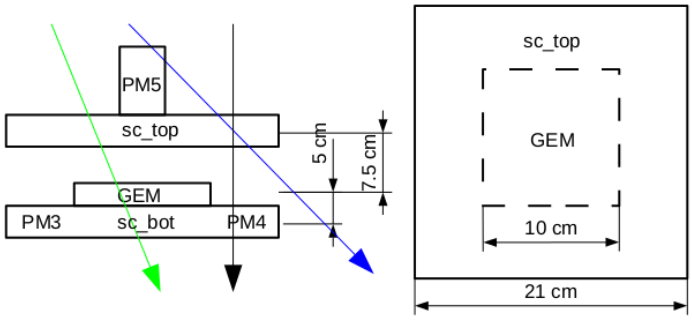

Figure 5.26 – In this scheme we see three possible paths for cosmic muons. The path in green hits all 3 detectors, the one in black hits only sc-top and sc-bot and the blue one hits only the scintillator on the top. Acceptance affects the measured detector efficiency and has to be taken into account.

5.5.1.3 Muons Rate Measurements

As a first step, to test the electronics setup and the Monte Carlo simulation, we measured the rate of cosmic muons which hit the top scintillator sc-top and the sc-bot. In section 5.5 we gave the expected rate for atmospheric muons and it was about 1 $cm^{-2}min^{-1}$. Hence on the top scintillator of 441 cm^2, we expect about 441 muons per

minute. Using the acceptance value of $\epsilon_{Acc} = 0.45 \pm 0.03$ for the geometrical configuration in use, we get an expected rate of 198 $\pm$ 13 muons per minute for muons passing through both top and bottom scintillators. The measurements give a value of 222 $\pm$ 3 muons compatible with 2 σ of the expected value. The slightly higher measurement rate could be explained by the presence of noise on each PM and especially due to the correlated noise observed between the two face-to-face, PM3 and PM4.

5.5.1.4 Triple-GEM prototype's efficiency results

In figure 5.27 we can see the efficiency curve for the triple-GEM prototype placed between the two scintillators. The plateau is reached at about 4800 V and this is higher than the value found in section 5.4 using photons. A possible explanation is the less number of primary electrons, produced by muons interacting with the gas mixture, in comparison with iron-55 photons. The number of primary electrons generated by muons can be estimated as follows:

$$n_T = \frac{\Delta E}{W_{Ar/CO_2}} = 100\, ion\, pairs/cm \tag{5.7}$$

where ΔE is the average energy loss by MIPs in the mixture of Ar/CO_2 70-30 %, W is the average value for the ionization energy in the mixture, see table 2.1.

Since the drift zone of the triple-GEM detector measures 3 mm, we estimate that 30 primary e^- are produced in that region. This number is much lower than 212 primary electrons generated by photons as discussed in section 5.3.1, therefore at the same gain the amount of electrons produced by the amplification is lower too and the noise might mask the signals produced by minimum ionizing energy muons. At -4800 V, higher gain allows to detect almost all cosmic muons.

In figure 5.27 the efficiency on the plateau is about 0.33 $\pm$ 0.01, this value has to be compared with the geometrical acceptance. In a such geometrical disposition not all muons hit the three detectors and in section 5.5.1.2 we estimated the geometrical acceptance: $\epsilon_{Acc} = 0.39 \pm 0.03$. Comparing this value with the one on the plateau we obtain an efficiency for the triple-GEM prototype of 0.85 ± 0.07.

This efficiency seems rather low in comparison with the 98 % obtained by other experiment using this kind of detector [23]. Therefore it is important to remind that this is the first attempt to measure this quantity at ULB with a completely new set-up, which is still in development. Despite our efforts to reduce the noise level, the threshold in use is still rather high compared with the primary charge released by MIPs. In the 3 mm thick drift zone of the triple-GEM prototype, a MIP produce about 30 primary e^-. In section 5.3 we measured the gain curve for the prototype and, for instance, at -4500 V we expect a gain of 8×10^3, so the average total number of electrons which induces the signal is:

$$30el \times 8 \times 10^3 = 2.4 \times 10^5 el \tag{5.8}$$

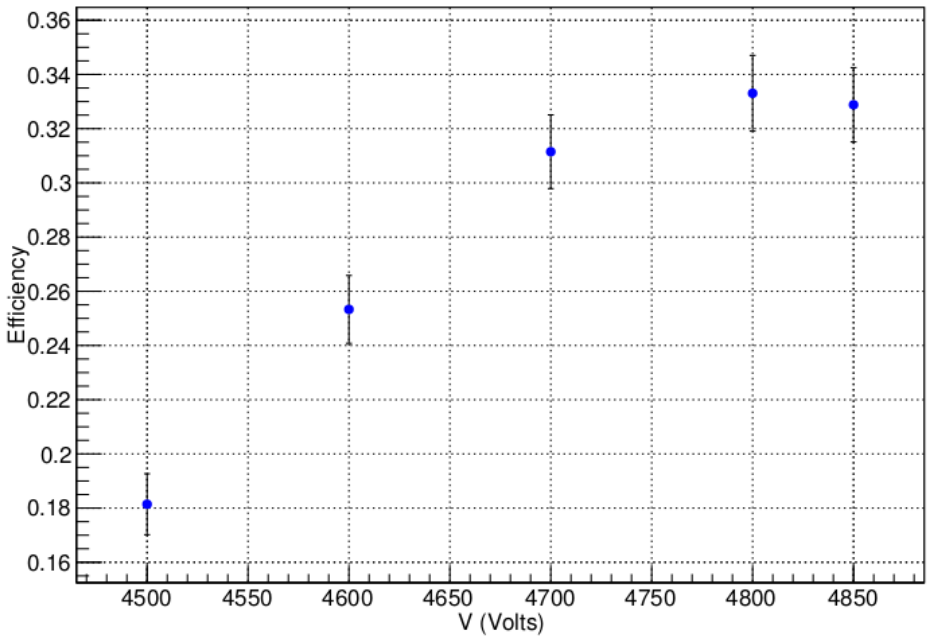

Figure 5.27 – Efficiency plateau obtained for the triple-GEM prototype placed between PM5 and PM3/4.

Now, using the calibration curve of section 5.3.2 we find:

$$2.4 \times 10^5 \times 4 \times 10^{-4} = 96mV \tag{5.9}$$

The average value of the output signal after the electronics amplification is only of 96 mV and it has to be compared with the threshold of 80 mV.

Consequently we estimate that the efficiency measurement is affected by the high noise. The Faraday cage that will be installed in the next future to shield the triple-GEM detector and the readout electronics should definitely improve the results.

Conclusion

This work aimed at the study of a small triple-GEM prototype in the framework of the upgrade of the CMS muon spectrometer. After the second long shutdown period of the LHC, the machine should reach a luminosity of $2 \times 10^{34}\ cm^{-2}s^{-1}$. At such value the rate and the particle fluxes will be a serious issue for the detectors currently in use. The triple-GEM detectors are the major candidates for the upgrade of the CMS muon spectrometre and many studies with small prototypes are necessary.

This work was conducted with a small triple-GEM prototype assembled by the ULB team. It has been tested at the ULB particle physics department, using a completely new set-up, still in development. After having mastered the cosmic arch set-up and the electronics, I calibrated the set-up and performed measurements of gain using a source of Fe^{55}. Gains higher than 10,000 have been measured and the detector is stable even at very high voltage and any spark breakdown has been observed.

The source of Fe^{55} allows to measure the efficiency curve for photons and permits to define the HV value at which the triple-GEM prototype begins to be fully efficient, around -4500 V. The efficiency curve presents a long plateau which confirms that the prototype is stable, also at very high voltage over several hundreds of volts.

Using the experimental set-up, and in particular the scintillators placed at the center of the cosmic arch, it is possible to exploit cosmic muons in order to measure the detector efficiency with charged particles. The efficiency curve shows the typical plateau but at higher gain compared to the photon efficiency curve. The plateau starts around -4800V and presents an efficiency value of 85 $\pm$ 7 %, lower of the expected 98 %. This can be explained taking into account the lower number of primary electrons generated in this case and the relevant signal-to-noise level. The installation of a Faraday cage in order to shield the prototype and the readout electronics should completely solve the issue.

Once the set-up will be completely finished with the Faraday cage and with new electronics, in order to readout each strips individually, the characterization will continue. In particular, the efficiency dependence on the incidence angle will be studied looking at the number of strips hit by the incoming cosmic muon.

Bibliography

[1] http://home.web.cern.ch/about.

[2] Lyndon R Evans and Philip Bryant. LHC Machine. *J. Instrum.*, 3:S08001, 2008.

[3] CMS Detector. `http://cms.web.cern.ch/news/cms-detector-design`, 2011.

[4] T. Bergauer. *Design, Construction and Commissioning of the CMS Tracker at CERN and Proposed Improvements for Detectors at the Future International Linear Collider*. PhD thesis, Vienna University of Technology, 2008.

[5] CERN Courier. `http://cerncourier.com/cws/article/cern/32915`, 2008.

[6] CMS Collaboration. Technical proposal for the upgrade of the CMS detector through 2020. Technical Report CERN-LHCC-2011-006. LHCC-P-004, CERN, Geneva, Jun 2011.

[7] *Technical proposal*. LHC Tech. Proposal. CERN, Geneva, 1994. Cover title : CMS, the Compact Muon Solenoid : technical proposal.

[8] Karol Bunkowski and Jan Krolikowski. *Optimization, Synchronization, Calibration and Diagnostic of the RPC PAC Muon Trigger System for the CMS detector*. PhD thesis, Warsaw U., Warsaw, 2009. Presented on Jul 2009.

[9] J P Koutchouk and F Zimmermann. LHC Upgrade Scenarios. (EuCARD-CON-2009-040. sLHC-PROJECT-Report-0013. CERN-sLHC-PROJECT-Report-0013. EuCARD-CON-2009-007), 2010.

[10] L. Rolandi W. Blum. *Particle Detection with Drift Chambers*. Springer Study Edition. Springer-Verlag, 1994.

[11] Fabio Sauli. Gaseous detectors fundaments. `https://indico.cern.ch/event/124394/contribution/0/material/slides/`, 2011.

[12] K. Nakamura et al.(Particle Data Group). Partial update for the 2012 edition. *J. Phys.*, G 37, 2010.

[13] Fabio Sauli. *Principles of operation of multiwire proportional and drift chambers*. CERN, Geneva, 1977.

[14] Serge Duarte Pinto. Micropattern gas detector technologies and applications, the work of the rd51 collaboration. `http://arxiv.org/abs/1011.5529`, 2010.

[15] Gas Detectors Development Group. `http://gdd.web.cern.ch/GDD`.

[16] Adam T. et al. The opera experiment target tracker. *Nucl.Instrum.Meth.*, A577:523–539, 2007.

[17] CAEN. *Mod.N470 4 channel programmable H.V. power supply manual.*

[18] CAEN. *Mod.N417 8 channel low threshold discriminator manual.*

[19] *Technical Information Manual, CAEN TDC Mod. V1290 A/N VX1290 A/N*, 2012.

[20] CAEN. *Mod. N93B dual timer manual.*

[21] CAEN. *Mod.N145 Quad Scaler and Preset Counter/Timer manual.*

[22] Glen Cowan. *Statistical data analysis.* University Press. Oxford science publications, Great Calendon Street, Oxford OX2 6DP, 1998.

[23] Andrey Marinov. *Feasibility Study of a GEM Based Muon System for the CMS Detector at the Large Hadron Collider.* PhD thesis, Universiteit Gent, Gent, 2013.

[24] *ORTEC 575A Amplifier Manual.*

[25] http://www.horiba.com/semiconductor/products/product-lines/mass-flow-controller/mass-flow-meter/.

[26] ORTEC. *Models 142A, 142B, and 142C Preamplifiers Operating and Service Manual.*

[27] Eric Harpell, Willy Langeveld, Don McShurley, Steve Shapiro, John Venuti. The CCRT: an inexpensive cosmic ray muon detector. *Standford Linear Accelerator Center.*